Element-Selective Molecular Charge Transport Characteristics of Binuclear Copper(II)-Lanthanide(III) Complexes

Sebastian Schmitz,[a] Andrew Kovalchuk,[b] Alejandro Martín-Rodríguez,[c]
Jan van Leusen,[a] Natalya V. Izarova,[d] Svenja D. M. Bourone,[a] Yong Ai,[b]
Eliseo Ruiz,[c,] Ryan C. Chiechi,[b,]* Paul Kögerler[a,d,]* and Kirill Yu. Monakhov[a,]**

[a] Institut für Anorganische Chemie, RWTH Aachen University, Landoltweg 1, 52074 Aachen, Germany. E-mails: kirill.monakhov@ac.rwth-aachen.de, paul.koegerler@ac.rwth-aachen.de

[b] Stratingh Institute for Chemistry & Zernike Institute for Advanced Materials, University of Groningen, Nijenborgh 4, Groningen 9747 AG, Netherlands. E-mail: r.c.chiechi@rug.nl

[c] Departament de Química Inorgànica i Orgànica and Institut de Química Teòrica i Computacional, Universitat de Barcelona, Diagonal 645, 08028 Barcelona, Spain. E-mail: eliseo.ruiz@qi.ub.edu

[d] Jülich-Aachen Research Alliance (JARA-FIT) and Peter Grünberg Institute (PGI-6), Forschungszentrum Jülich, 52425 Jülich, Germany.

Contents

1. Synthesis and characterization of compound 6

Method a:

HL·SMe (0.137 g, 0.50 mmol) was dissolved in 10 mL of methanol, and triethylamine (0.08 mL, 0.58 mmol) was added. The mixture was stirred at 80 °C for 10 min, followed by the addition of $CuX_2{\cdot}nH_2O$ (here: $[Cu_2(OOCMe)_4(H_2O)_2]$; 0.10 g, 0.25 mmol) which immediately resulted in a color change from orange to dark brown. The resulting solution was stirred under reflux conditions for one hour. Dark-brown single crystals of $[Cu(L{\cdot}SMe)_2]$ (compound **6**) were obtained after one day; they were washed with a small amount of ice-cold methanol and dried in air.

Method b:

$Cu(hfa)_2{\cdot}xH_2O$ (hfa = hexafluoroacetylacetonate) (0.124 g, 0.25 mmol; for x = 1), $Dy(acac)_3{\cdot}xH_2O$ (acac = acetylacetonate) (0.119 g, 0.25 mmol; for x = 1) and the Schiff base ligand HL·SMe (0.137 g, 0.50 mmol) were dissolved together in 10 mL of methanol, and triethylamine (0.08 mL, 0.58 mmol) was added. The mixture was stirred under reflux conditions for one hour. Dark-brown single crystals of compound **6** were obtained after one day; they were washed with a small amount of ice-cold methanol and dried in air.

Elemental analysis, calcd. for $C_{30}H_{28}CuN_2O_4S_2$ (608.20 g mol^{-1}): C, 59.24; H, 4.64 and N, 4.61 %. Found: C, 59.15; H, 4.54 and N, 4.48 %.

IR: $\tilde{\nu}_{max}$(KBr pellet) / cm^{-1}: 3429 (w, br), 3046 (w), 2999 (w), 2915 (w), 2833 (w), 1600 (vs), 1581 (sh), 1541 (s), 1489 (m), 1464 (sh), 1439 (s), 1377 (m), 1355 (w), 1330 (m), 1249 (s), 1239 (sh), 1191 (vs), 1180 (sh), 1105 (m), 1077 (m), 1013 (m), 984 (m), 870 (w), 855 (m), 827 (m), 782 (w), 739 (s), 729 (sh), 715 (sh), 612 (vw), 586 (m), 526 (w), 488 (w), 441 (m).

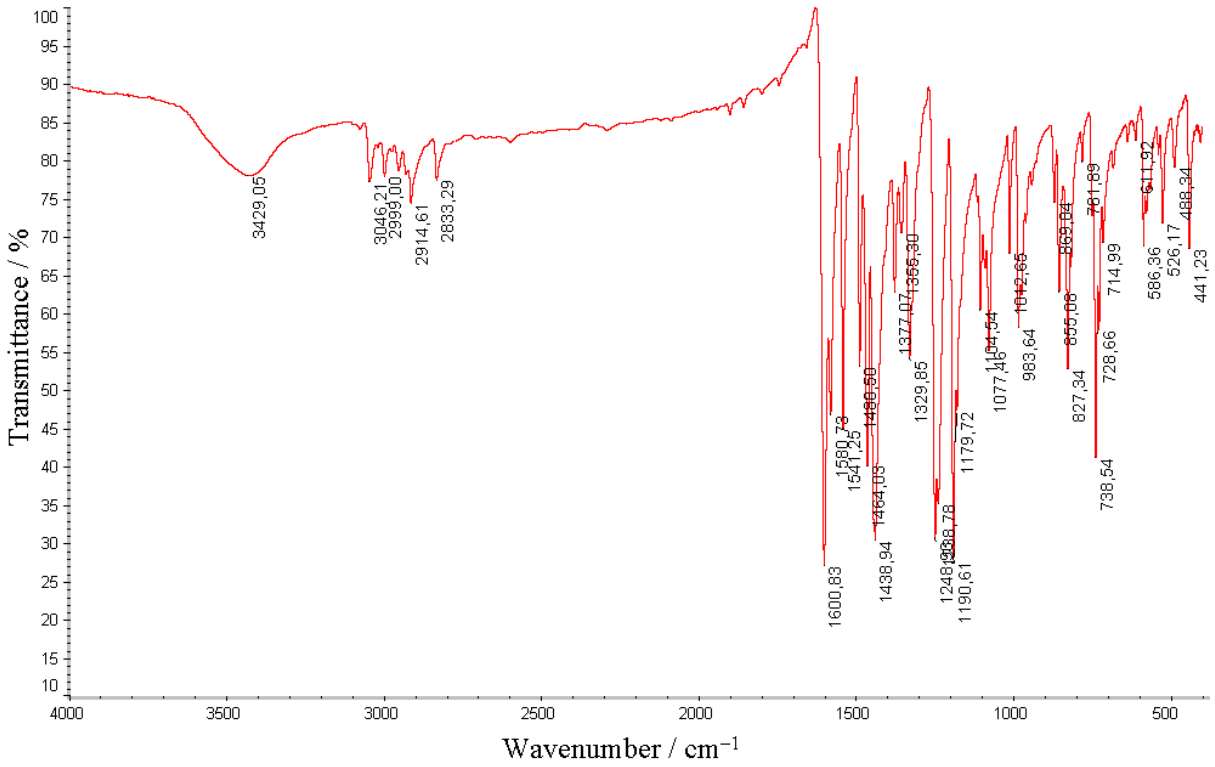

Fig. S1 IR spectrum of compound **6** measured in the 4000–450 cm^{-1} region, using a KBr pellet.

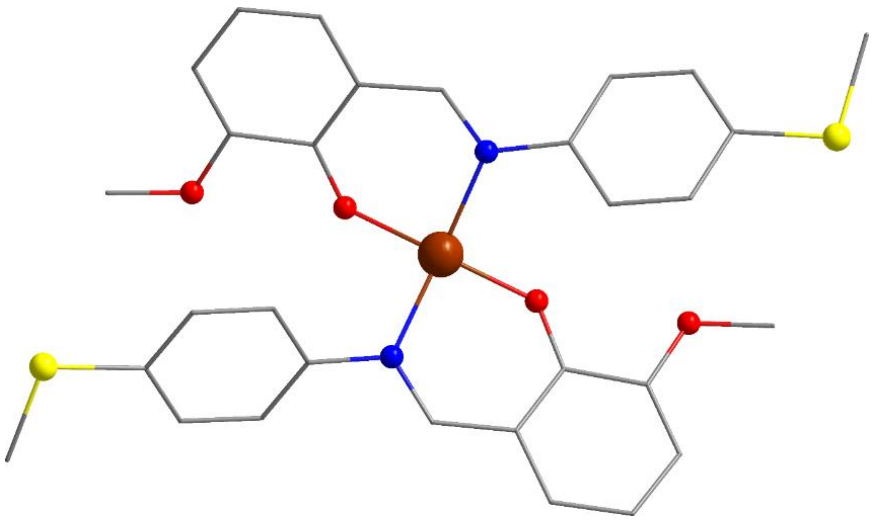

Fig. S2 Molecular structure of compound **6**. Hydrogen atoms are omitted for clarity. Color code: C, gray; N, blue; O, red; S, yellow; Cu, brown.

The SQUID measurements of **6** yield the magnetic data shown in Fig. S3. At 290 K and 0.1 T, the $\chi_m T$ value of 0.42 $cm^3\ K\ mol^{-1}$ lies within the expected range for a single Cu^{2+} center (0.36–0.61 $cm^3\ K\ mol^{-1}$ [1]). By cooling the compound, $\chi_m T$ slowly decreases to 0.40 $cm^3\ K\ mol^{-1}$ at 25.0 K, and subsequently sharply drops to 0.36 $cm^3\ K\ mol^{-1}$ at 2.0 K. Taking into account the tetragonal strongly distorted tetrahedral coordination geometry, which generates a well isolated Kramers doublet, and the small Zeeman effect generated by the applied field of 0.1 T, this distinct drop off indicates the presence of antiferromagnetic exchange interactions. The exchange interactions are of inter-molecular nature, since the shortest distance between two Cu^{2+} centers of two molecules of **6** is 6.057 Å according to the single crystal structure, i.e. an even shorter distance between two copper centers than in **5**. The molar magnetization at 2.0 K is linear in B up to approximately 1.5 T, and reaches a value of 0.96 $N_A\ \mu_B$ at 5.0 T without being saturated.

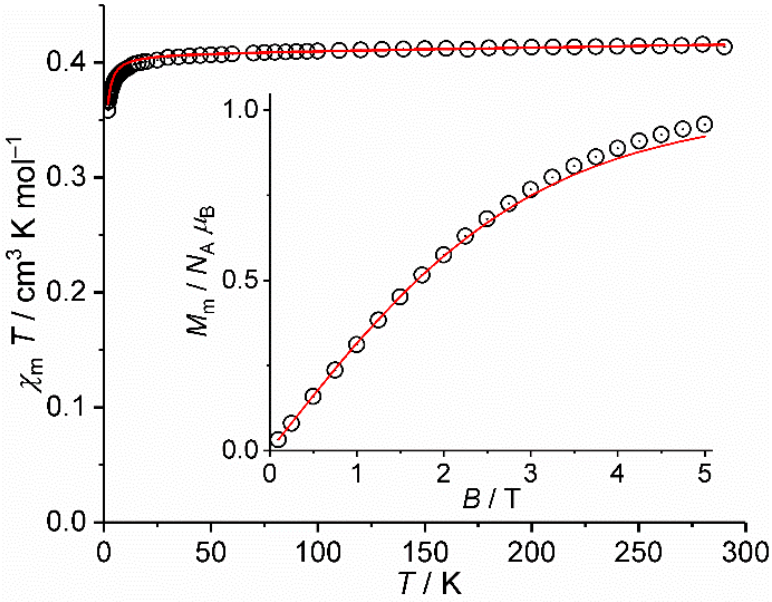

Fig. S3 Temperature dependence of $\chi_m T$ at 0.1 T**,** and field dependence of the molar magnetization M_m at 2.0 K (inset) of **6**; open symbols: experimental data; solid lines: least–squares fits.

The data are modeled employing the computational framework CONDON.[2,3] As for **5**, we assumed a ligand field symmetry of approximately D_{2d} to describe the coordination geometry of **6** as tetragonal distorted tetrahedron. The PCEM was used to generate starting values for the ligand field parameters, and the full basis of the $3d^9$ electron configuration (10 energy states) was taken into account during the calculations. A mean-field approach was adopted to consider potential inter-molecular exchange interactions. The parameters of the least-squares fit of SQ = 1.4 % are listed in Table S1. The ligand field parameters are related to those of **5**, yet slightly varied due to the different arrangement of the N and O ligands. The inter-molecular exchange interactions characterized by zJ' are very weak and antiferromagnetic.

Table S1 Magnetic quantities and fit parameters of **6**: one electron spin-orbit coupling constant ζ, Racah parameters *B* and *C*, ligand field parameters B^k_q in Wybourne notation, mean-field parameter (*zJ'* in "–2*J*" notation).

	Cu^{2+} (**6**)
ζ / cm^{-1} [4]	829
B / cm^{-1} [4]	1238
C / cm^{-1} [4]	4659
B^2_0 / cm^{-1}	–23157 ± 2653
B^4_0 / cm^{-1}	21959 ± 1474
B^4_4 / cm^{-1}	–49709 ± 10677
zJ' / cm^{-1}	–0.30 ± 0.05
SQ	1.4 %

2. Analytical data of HL·SMe

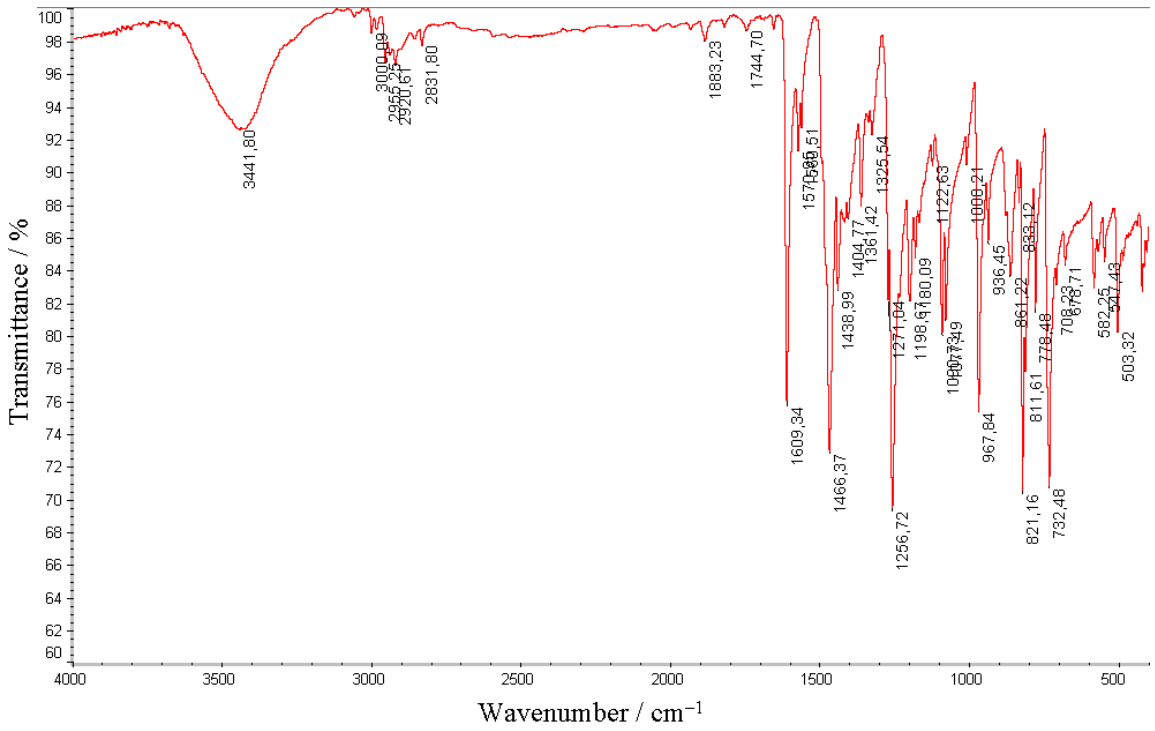

Fig. S4 IR spectrum of HL·SMe measured in the 4000–450 cm^{-1} region, using a KBr pellet.

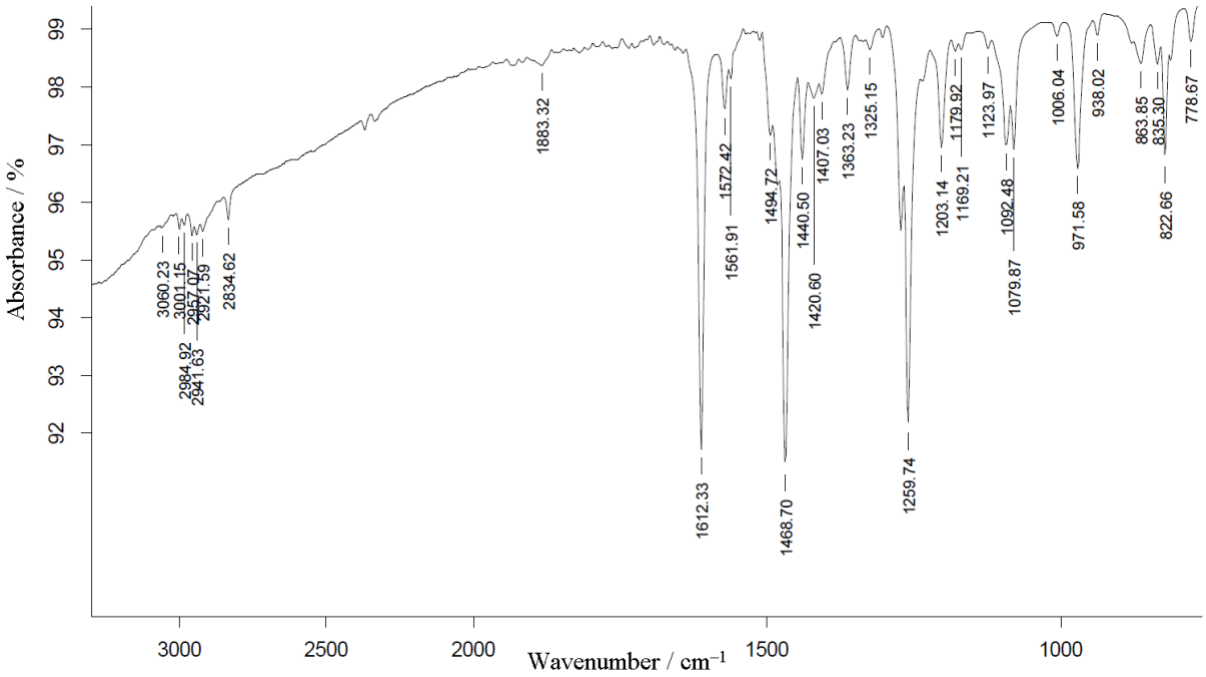

Fig. S5 IRRAS spectrum of HL·SMe immobilized on a gold substrate from a 1.0 mmolar ethanolic solution.

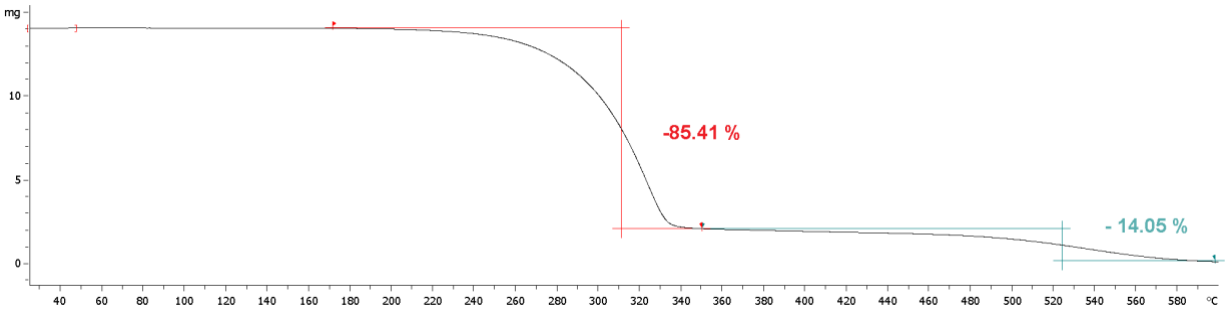

Fig. S6 TGA curve of HL·SMe measured in dry air.

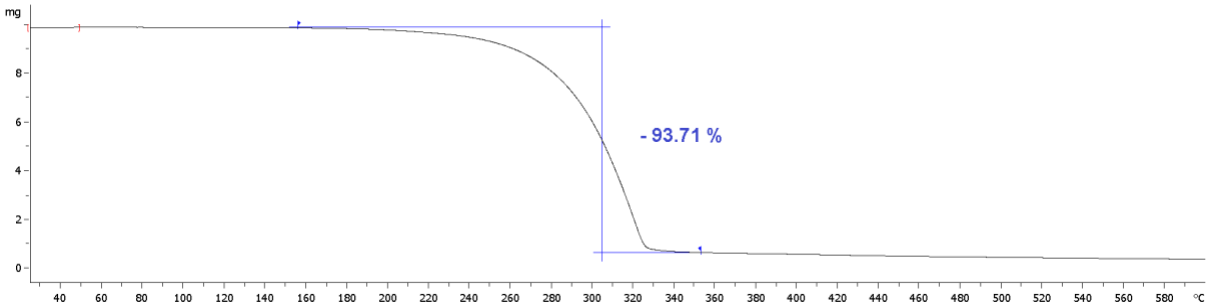

Fig. S7 TGA curve of HL·SMe measured under nitrogen atmosphere.

3. IR spectra of compounds 1–5 and IRRAS spectra of compound 2

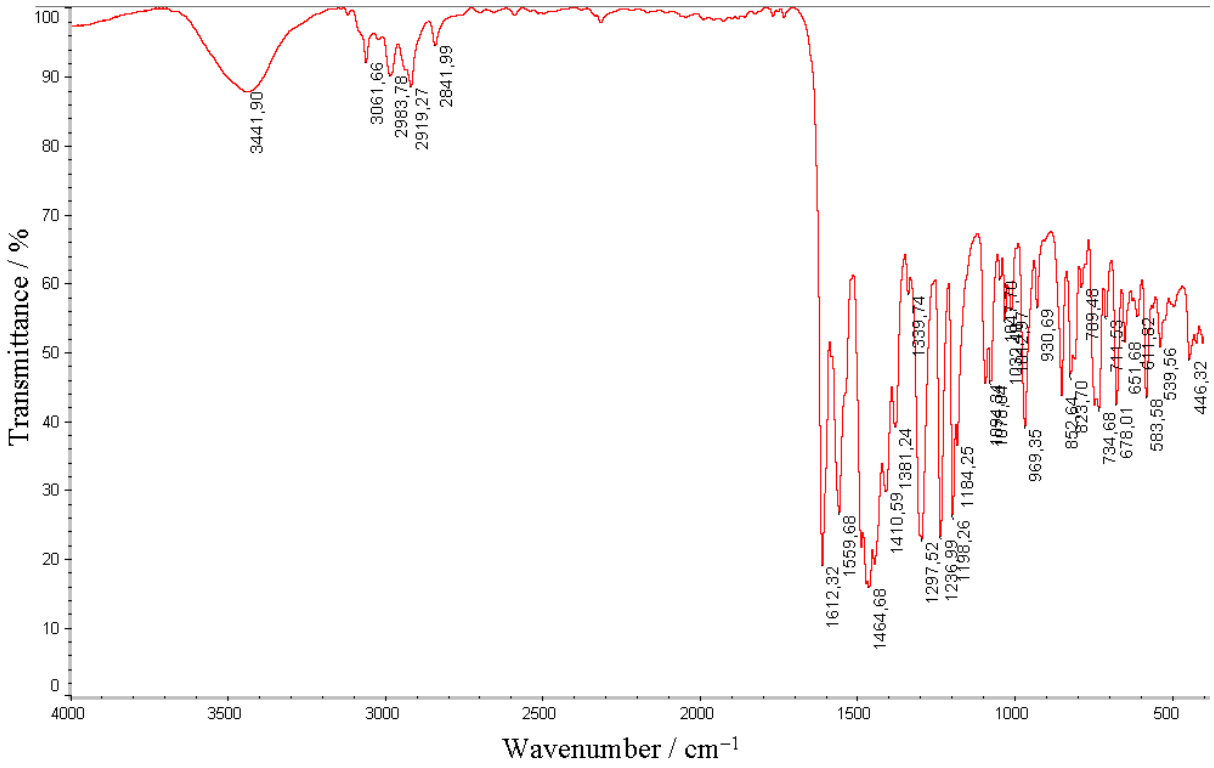

Fig. S8 IR spectrum of compound **1** measured in the 4000–450 cm^{-1} region, using a KBr pellet.

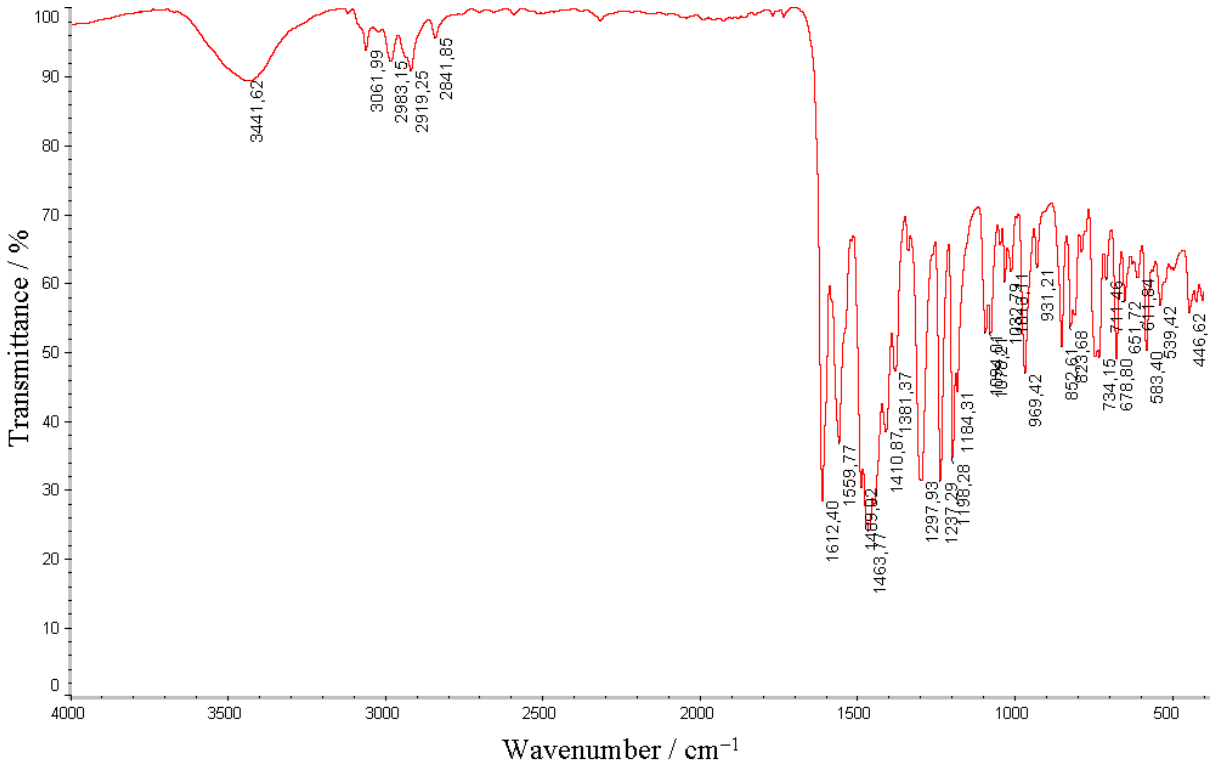

Fig. S9 IR spectrum of compound **2** measured in the 4000–450 cm^{-1} region, using a KBr pellet.

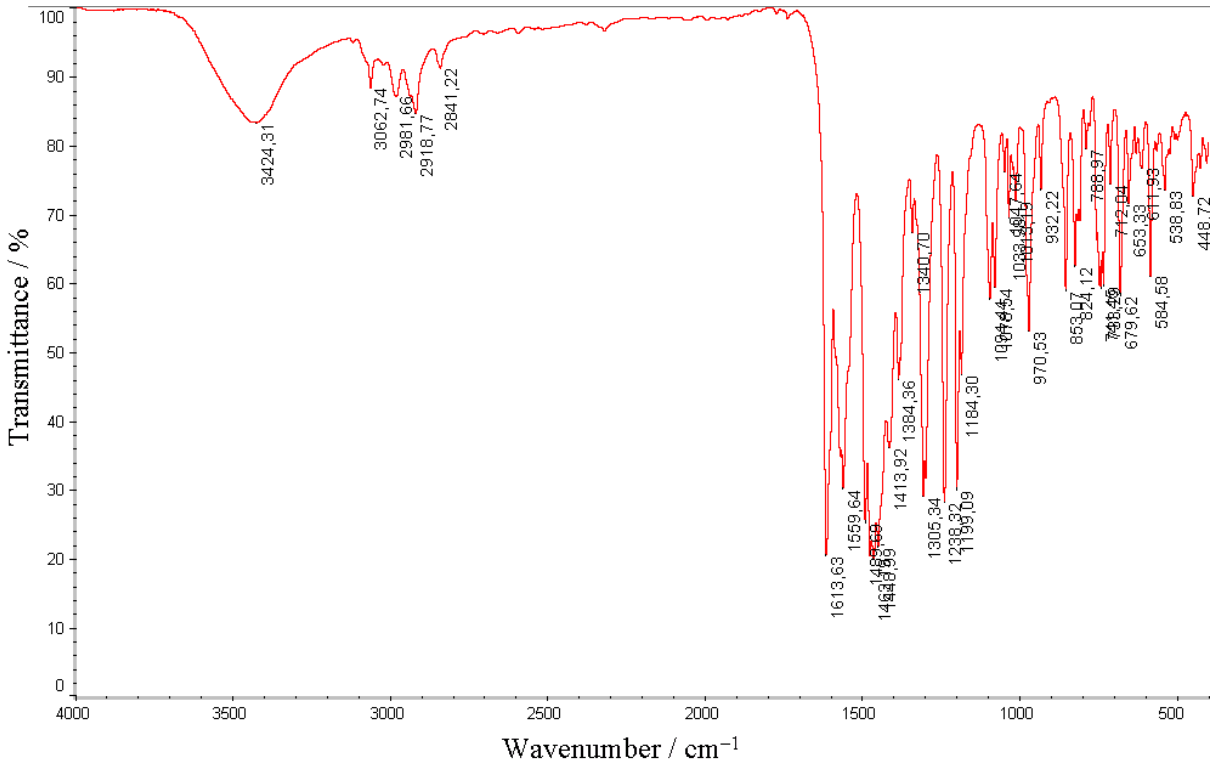

Fig. S10 IR spectrum of compound **3** measured in the 4000–450 cm^{-1} region, using a KBr pellet.

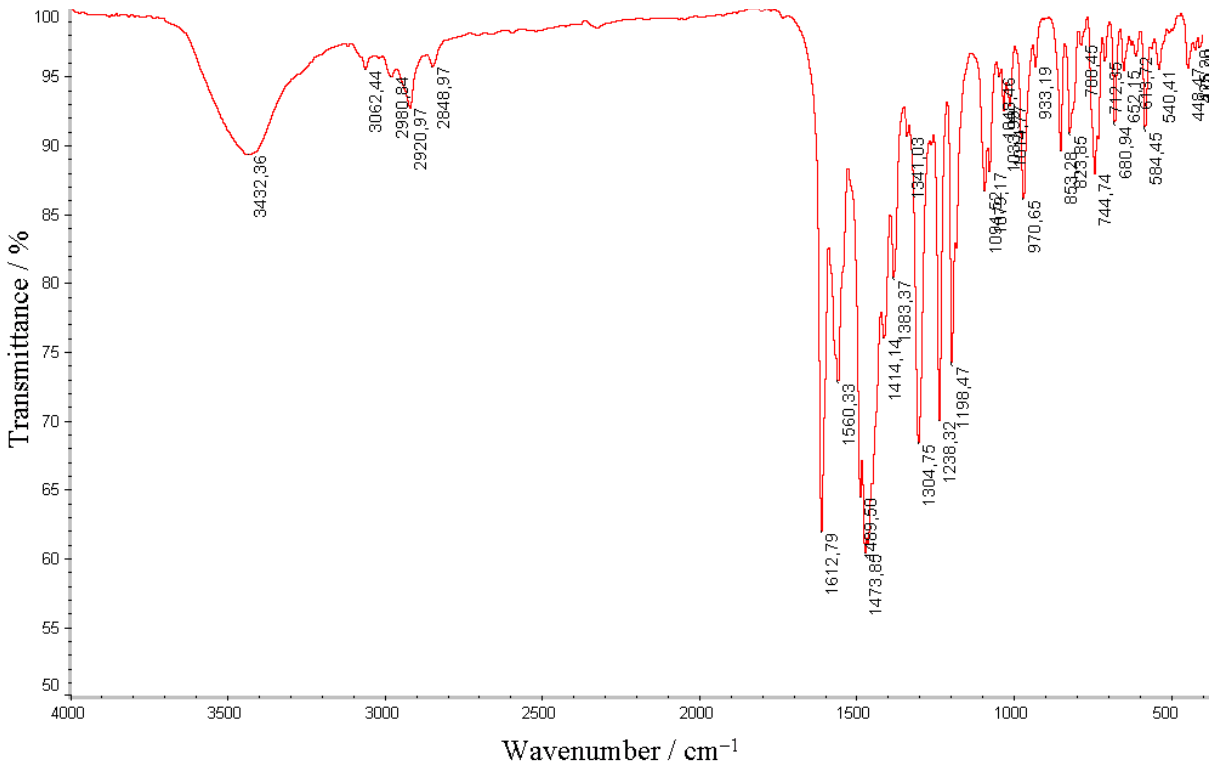

Fig. S11 IR spectrum of compound **4** measured in the 4000–450 cm^{-1} region, using a KBr pellet.

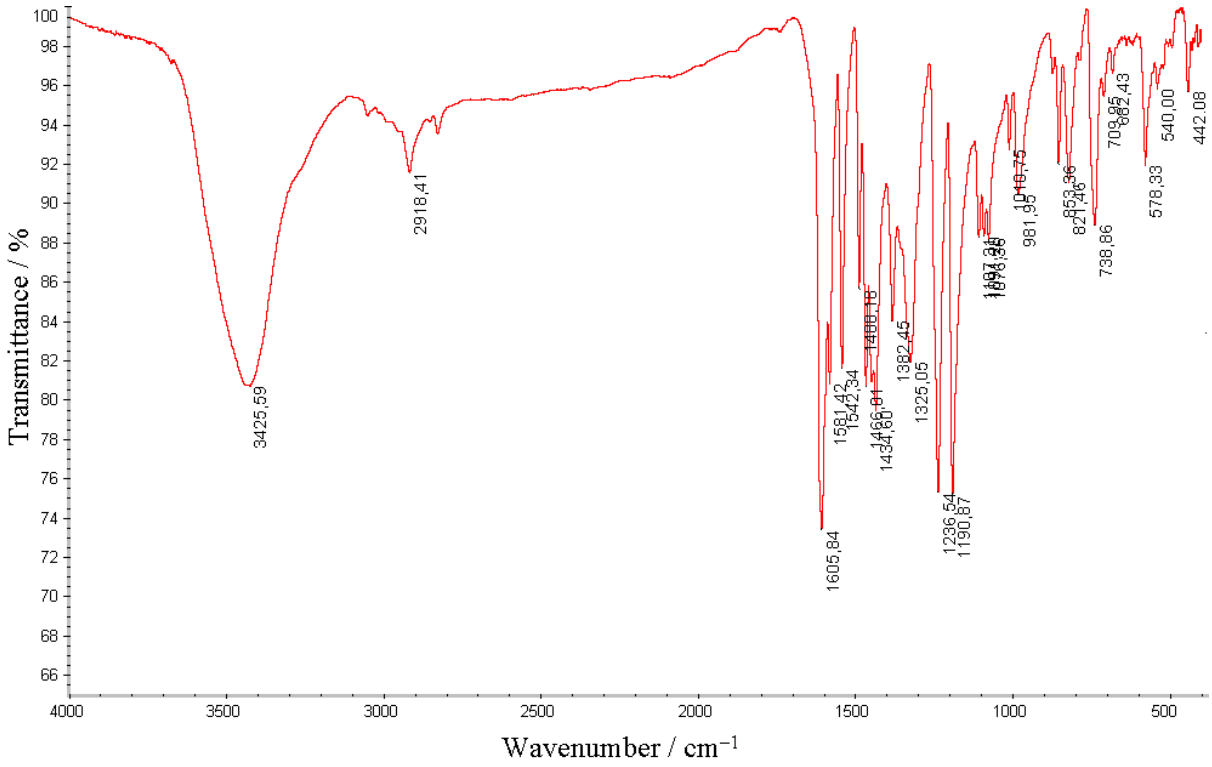

Fig. S12 IR spectrum of compound **5** measured in the 4000–450 cm^{-1} region, using a KBr pellet.

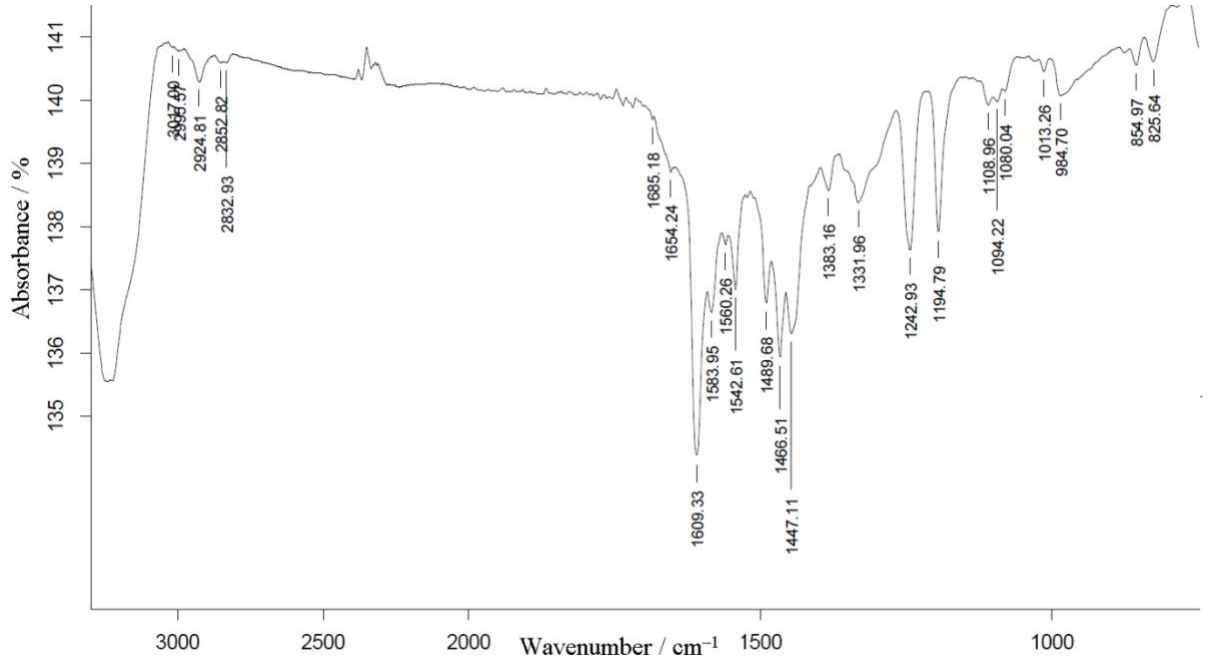

Fig. S13 IRRAS spectrum of compound **2** (washed dropewise with MeOH).

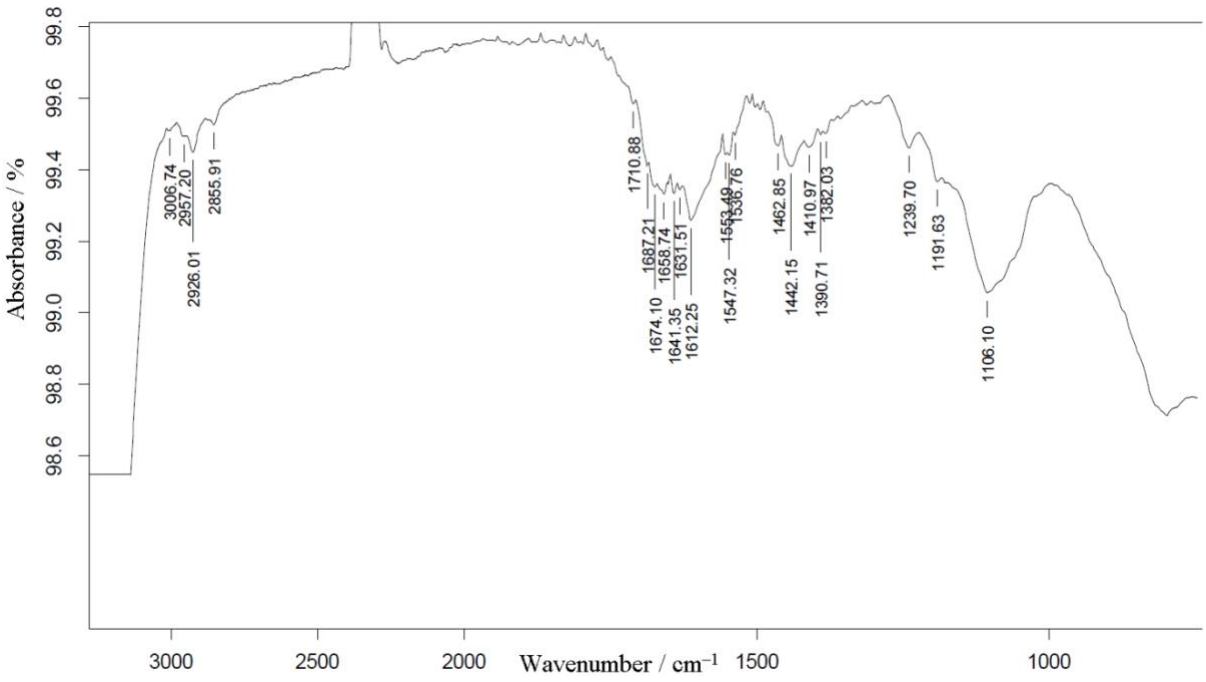

Fig. S14 IRRAS spectrum of compound **2** after dipping in MeOH (washed more intense).

4. Crystal data and structure refinement details for compounds 1–6 and HL·SMe

Table S2 Crystal data and structure refinement for **1**–**3**.

Sample	**1**	**2**	**3**
Radiation type	Mo Kα	Mo Kα	Mo Kα
Empirical formula	$C_{35}H_{37}CuGdN_3O_{12}S_2$	$C_{35}H_{37}CuN_3O_{12}S_2Tb$	$C_{34.75}H_{37}CuDyN_3O_{11.75}S_2$
Formula weight, g/mol	976.59	978.26	974.83
Crystal system	Triclinic	Triclinic	Triclinic
Space group	*P*–1	*P*–1	*P*–1
a / Å	10.4420(15)	10.41025(18)	10.2537(4)
b / Å	12.9883(19)	13.0045(3)	13.0750(5)
c / Å	14.766(2)	14.8408(2)	15.0238(5)
α	110.052(3)	110.2260(19) °	110.534(3) °
β	90.300(3)	90.3313(14) °	90.219(3) °
γ	94.099(3)	93.9638(16) °	93.063(3) °
Volume / Å^3	1875.5(5)	1879.79(7)	1882.98(13)
Z	2	2	2
D_{calc}, g/cm^3	1.729	1.728	1.719
Absorption coefficient, mm^{-1}	2.497	2.609	2.709
F(000)	978	980	975
Crystal size, mm	0.17 × 0.27 × 0.32	0.11 × 0.35 × 0.43	0.15 × 0.25 × 0.28
Theta range for data collection	1.67° – 23.32°	3.15° – 26.02°	3.41° – 26.02°
Completeness to Θ_{max}	99.6 %	99.8 %	99.6 %
Index ranges	–11 < *h* < 11, –14 < *k* < 14, –16 < *l* < 16	–12 < *h* < 12, –16 < *k* < 16, –18 < *l* < 18	–12 < *h* < 12, –16 < *k* < 16, –18 < *l* < 18
Reflections collected	26294	37878	37026
Independent reflections	5418	7400	7389
R_{int}	0.0984	0.0545	0.0557
Observed ($I > 2\sigma(I)$)	4767	6626	6042
Absorption correction	Semi-empirical from equivalents	Analytical numerical using a multifaceted crystal model	
T_{min} / T_{max}	0.3551 / 0.6762	0.2506 / 0.7661	0.4209 / 0.6829
Data / restraints / parameters	5418 / 12 / 505	7400 / 0 / 505	7389 / 18 / 548
Goodness-of-fit on F^2	1.019	0.994	1.055
R_1, wR_2 ($I > 2\sigma(I)$)	R_1 = 0.0397, wR_2 = 0.0914	R_1 = 0.0275, wR_2 = 0.0651	R_1 = 0.0436, wR_2 = 0.1012
R_1, wR_2 (all data)	R_1 = 0.0471, wR_2 = 0.0964	R_1 = 0.0343, wR_2 = 0.0699	R_1 = 0.0623, wR_2 = 0.1159
Largest diff. peak and hole / e Å^{-3}	0.730 / –1.352	0.7571 / –0.558	2.422 / –1.621

Table S3 (continuation) Crystal data and structure refinement for **4**–**6** and HL·SMe.

Sample	**4**	**5**	**6**	**HL·SMe**
Radiation type	Cu Kα	Mo Kα	Mo Kα	Mo Kα
Empirical formula	$C_{35}H_{37}CuN_3O_{12}S_2Y$	$C_{63}H_{68}Cu_2N_5NaO_{14}S_4$	$C_{30}H_{28}CuN_2O_4S_2$	$C_{15}H_{15}NO_2S$
Formula weight, g/mol	908.25	1397.53	608.20	273.34
Crystal system	Triclinic	Monoclinic	Monoclinic	Orthorhombic
Space group	*P*–1	$P2_1/c$	$P2_1/c$	$P2_12_12_1$
a / Å	10.4154(3)	14.9698(3)	13.6389(4)	6.47212(10)
b / Å	13.0079(4)	24.2955(4)	15.8734(5)	11.17376(19)
c / Å	14.8097(5)	20.7256(5)	13.4847(4)	18.3473(2)
α	110.182(3)	90 °	90 °	90 °
β	90.353(2)	110.749(3) °	114.537(4) °	90 °
γ	93.981(2)	90 °	90 °	90 °
Volume / Å^3	1877.74(11)	7049.0(2)	2655.75(16)	1326.84(3)
Z	2	4	4	4
D_{calc}, g/cm^3	1.606	1.317	1.521	1.368
Absorption coefficient, mm^{-1}	4.372	0.790	1.021	0.241
F(000)	928	2904	1260	576
Crystal size, mm	0.08 × 0.16 × 0.41	0.12 × 0.45 × 0.75	0.18 × 0.39 × 0.61	0.09 × 0.22 × 0.50
Theta range for data collection	7.44° – 68.25°	4.12° – 26.02°	3.53° – 25.68°	4.26° – 26.37°
Completeness to Θ_{max}	96.0 %	99.5 %	99.8 %	99.4 %
Index ranges	–12 < *h* < 12, –15 < *k* < 15, –17 < *l* < 17	–18 < *h* < 18, –29 < *k* < 29, –25 < *l* < 25	–16 < *h* < 16, –19 < *k* < 19, –16 < *l* < 16	–8 < *h* < 8, –13 < *k* < 13, –22 < *l* < 22
Reflections collected	30628	73696	26616	13871
Independent reflections	6623	13844	5030	2688
R_{int}	0.1005	0.0626	0.0578	0.0342
Observed ($I > 2\sigma(I)$)	5877	10037	4159	2476
Absorption correction	Numerical based on gaussian integration over a multifaceted crystal model	Analytical numerical using a multifaceted crystal model	Numerical based on gaussian integration over a multifaceted crystal model	Analytical numerical using a multifaceted crystal model
T_{min} / T_{max}	0.1918 / 0.7267	0.9113 / 0.9122	0.0518 / 0.8360	0.3737 / 0.9779
Data / restraints / parameters	6623 / 0 / 505	13844/ 43 / 838	5030 / 0 / 352	2688 / 0 / 172
Goodness-of-fit on F^2	1.040	0.976	1.056	1.047
R_1, wR_2 ($I > 2\sigma(I)$)	R_1 = 0.0673, wR_2 = 0.1701	R_1 = 0.0636, wR_2 = 0.1817	R_1 = 0.0593, wR_2 = 0.1540	R_1 = 0.0283, wR_2 = 0.0693
R_1, wR_2 (all data)	R_1 = 0.0727, wR_2 = 0.1784	R_1 = 0.0929, wR_2 = 0.2101	R_1 = 0.0704, wR_2 = 0.1678	R_1 = 0.0326, wR_2 = 0.0722
Largest diff. peak and hole / e Å^{-3}	1.701 / –1.172	1.451 / –0.743	3.613 / –0.658	0.159 / –0.245

5. A comparative analysis of structural data between compounds 1–5 and related complexes described in the literature

Table S4 Selected bond metrics for compounds **1**–**4**.

Bond	Distances in Å			
	Ln = Gd (1)	**Ln = Tb (2)**	**Ln = Dy (3)**	**Ln = Y (4)**
Ln–$O_{acetate}$ (bridging)	2.316(4)	2.290(2)	2.275(4)	2.267(3)
Ln–$O_{acetate}$ (chelating)	2.432(4) – 2.476(4)	2.404(2) – 2.463(2)	2.396(4) – 2.443(4)	2.381(3) – 2.449(3)
Ln–O_{nit}	2.508(4) – 2.517(4)	2.489(3) – 2.513(2)	2.473(4) – 2.515(5)	2.469(3) – 2.476(3)
Ln–O_{ether}	2.474(4) – 2.578(4)	2.466(2) – 2.581(2)	2.463(4) – 2.573(4)	2.439(3) – 2.567(3)
Ln–O_{alc}	2.302(4) – 2.353(4)	2.292(2) – 2.347(2)	2.292(4) – 2.344(4)	2.267(3) – 2.318(3)
Cu–$O_{acetate}$	2.196(4)	2.196(2)	2.209(4)	2.192(3)
Cu–O_{alc}	1.957(4) – 1.962(4)	1.953(2) – 1.969(2)	1.958(4) – 1.964(4)	1.964(3) – 1.970(3)
Cu–N_{imi}	1.998(5) – 2.012(4)	1.997(3) – 2.017(3)	2.002(5) – 2.019(5)	2.006(3) – 2.022(3)
$Ln_{intra}\cdots Cu_{intra}$	3.3960(8)	3.3832(4)	3.3870(8)	3.3605(6)
$Cu_{intra}\cdots S_{intra}$	7.10	7.10	*disorder*	*disorder*

Only three {CuY} complexes supported by Schiff base ligands are reported in the Cambridge Structural Database (CSD).[5,6,7] In those compounds, the *copper(II) ions* show a *square-planar* coordination environment and the *yttrium(III) ions* are coordinated by *eight oxygen atoms*. This is different from the situation in compound **4** where the *copper(II) ion* exhibits a *square-pyramidal* geometry and the *yttrium(III) ion* is coordinated by *nine oxygen atoms* (see Table S4). Complexes described in the literature consist of one Schiff base ligand (salen or saloph) and three hexafluoroacetylacetonate (hfa) co-ligands which saturate the coordination environment of yttrium. In comparison, compound **4** contains two Schiff base ligands, one bridging acetate, one chelating acetate and one chelating nitrate.

A {CuDy} complex similar to compound **3** was published by Zhang *et al.* in 2013.[8] The metal ions in that complex show the same coordination environment (see Table S5), i.e. they are bridged by one acetate ligand, and an acetate and a nitrate are at Dy. Contrary to compound **3** with two thioether-augmented Schiff base ligands, the complex described in the literature is supported by only one *o*-vanillin salen Schiff base ligand (H_2L^1 see Fig. S15).

A search for 3d-4f complexes with the "non-functionalized" Schiff base ligand (HL) such as phenol-2-methoxy-6-[(*E*)-(phenylimino)methyl] gave two hits[9,10] in the Cambridge Structural Database. In 2014 Upadhyay *et al.* reported a dinuclear {ZnDy} complex[9]

([ZnDy(L^2)$_2$(OOCMe)(NO_3)$_2$]; HL^2 = Schiff base ligand; see Fig. S15) which is *quasi*-isostructural to compound **3** (see Table S5). A minor difference can be observed in the coordination of chelating ligands at Dy: two nitrate ions in the {ZnDy} complex and one nitrate / one acetate in compound **3**. Another related example is however a linear trinuclear {Ni_2Gd} complex[10] ([$Ni_2Gd(L^2)_6$]NO_3; HL^2 = Schiff base ligand) which is mono-cationic (see Table S5). In this complex, the nickel atoms are in an octahedral N_3O_3 coordination environment and gadolinium exhibits an icosahedral geometry.

Table S5 Coordination number (CN) of metal ions in compounds **1**–**4** (see *this work*) and in the reported, related coordination complexes. Distances (in Å) between 3d ions and Ln/Y ions in these heterometallic compounds are given.

Reference	Formula	CN of 3d	CN of Ln and Y	3d···Ln/Y distance
this work	[CuLn(L·SMe)$_2$(OOCMe)$_2$(NO_3)]	5	9	3.361 – 3.396
[5]	[CuY(hfa)$_3$(salen)]	4	8	3.275
[6]	[CuY(hfa)$_3$(saloph)]	4	8	3.201
[8]	[CuDy(L^1)(OOCMe)$_2$(NO_3)]	5	9	3.326
[9]	[ZnDy(L^2)$_2$(OOCMe)(NO_3)$_2$]	5	9	3.431
[10]	[$Ni_2Gd(L^2)_6$]NO_3	6	12	3.325

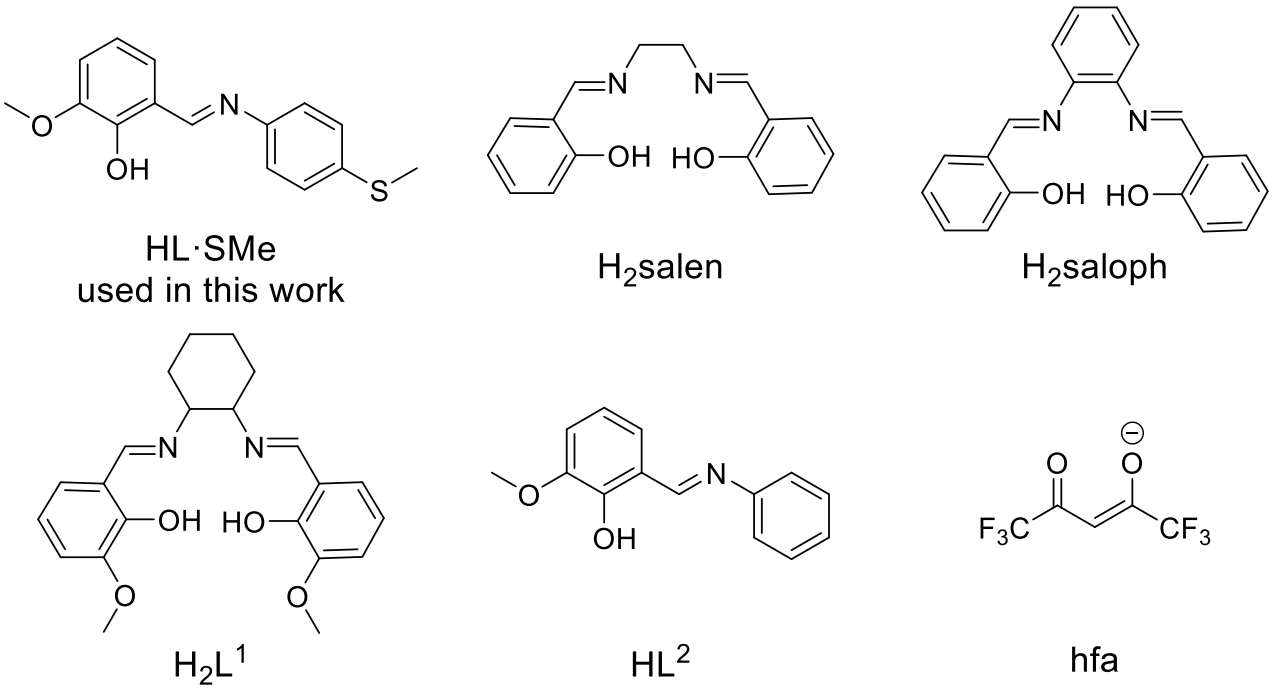

Fig. S15 Ligands present in compounds listed in Table S5.

The Cambridge Structural Database shows twelve hits for Schiff base-supported {CuNaCu} complexes.[11,12,13,14,15,16,17] Interestingly, ten of those twelve reported complexes contain perchlorate as counter-ion (4 hits) or coordinated to the central sodium ion (6 hits). Only in two other cases, the metal ions are characterized by a coordination environment identical to that in compound **5** (see Table S6). In 2013 Maiti *et al.* published a complex[15] with the formula $[Cu_2Na(Lig^1)_2]ClO_4{\cdot}0.5H_2O$ (H_2Lig^1 = *N*,*N*´-Bis(3-methoxysalicylidenimino)-1,3-diaminopentane; see Fig. S16). The Cu···Cu distance and the Cu–Na–Cu angle in this complex are 7.001 Å and 174.64(3)°, respectively. In 2013 Biswas *et al.* published another {CuNaCu} complex[16] with the formula $[Cu_2Na(Lig^2)_2]ClO_4{\cdot}CH_3COCH_3$ (H_2Lig^2 = 3-methoxysalicylaldehyde-diamine, with *trans*-1,2-diaminocyclohexane as diamine moiety; see Fig. S16). The Cu···Cu distance and the Cu–Na–Cu angle in this complex are 6.837 Å and 166.991(80)°, respectively. These reported Cu···Cu distances are slightly longer than that (6.813 Å) in compound **5** with a nearly perfect linear metal core (Cu–Na–Cu angle = 178.74(6)°).

Table S6 Comparison between selected structural data of compound **5** (see *this work*) and the reported, related coordination complexes.

Reference	**Formula**	**Cu···Cu distance** (in Å)	**Cu···Na distance** (in Å)	**Cu–Na–Cu angle** (in °)
this work	$[Cu_2Na(L{\cdot}SMe)_4]NO_3$	6.813	3.406 and 3.408	178.75
[15]	$[Cu_2Na(Lig^1)_2]ClO_4$	7.001	3.499 and 3.510	174.64
[16]	$[Cu_2Na(Lig^2)_2]ClO_4$	6.837	3.433 and 3.448	166.99

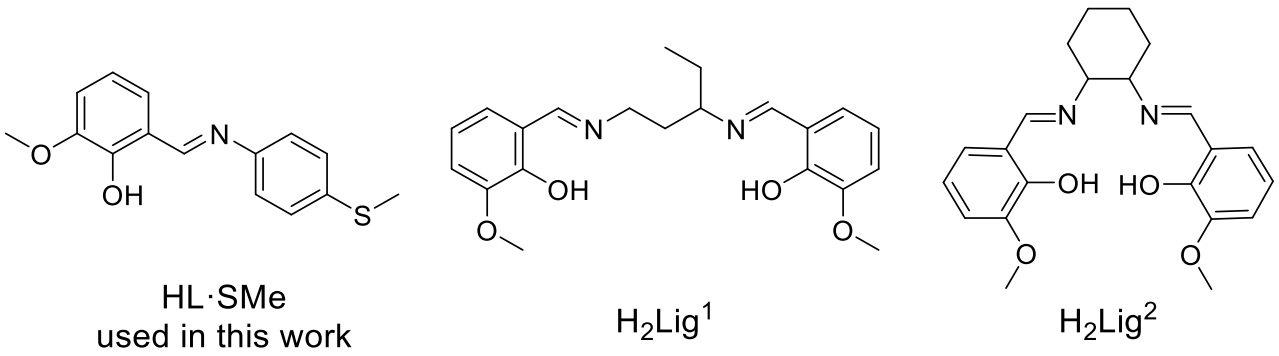

Fig. S16 Ligands present in compounds listed in Table S6.

6. Measured ESI-MS spectra of compounds 1–5

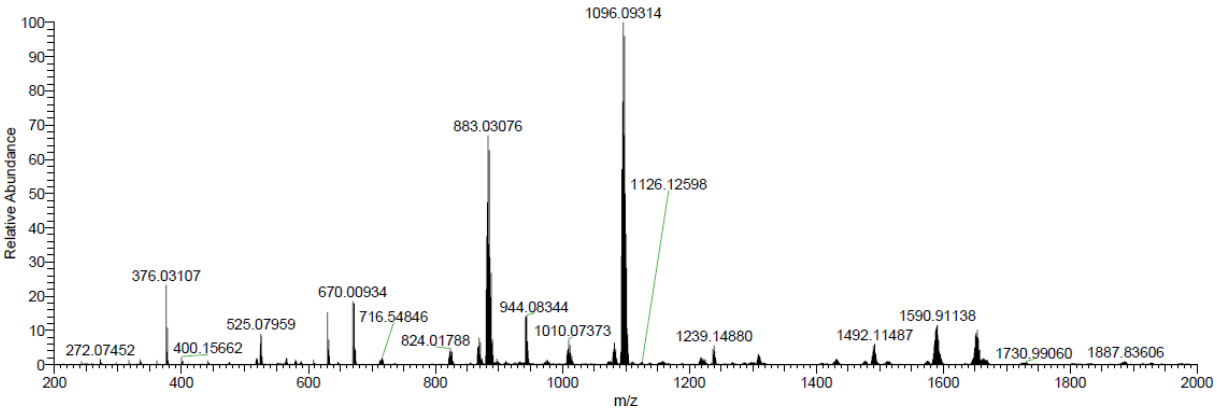

Fig. S17 ESI-MS spectrum of compound **1** in the positive ion mode.

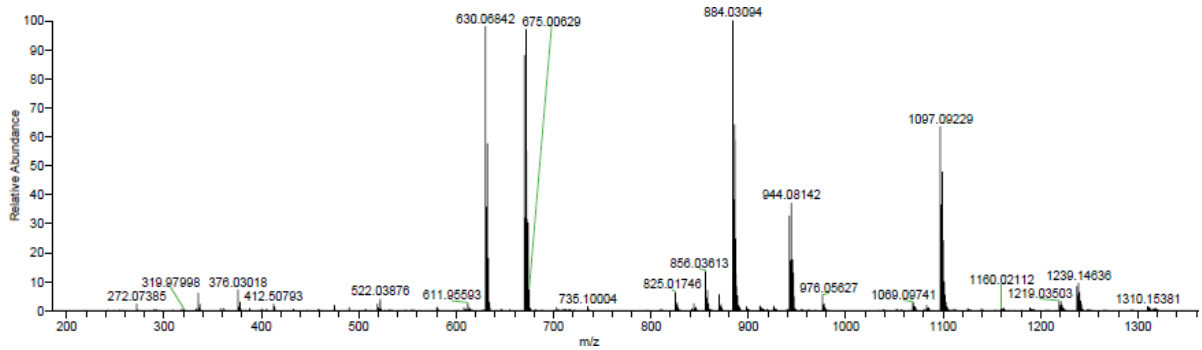

Fig. S18 ESI-MS spectrum of compound **2** in the positive ion mode.

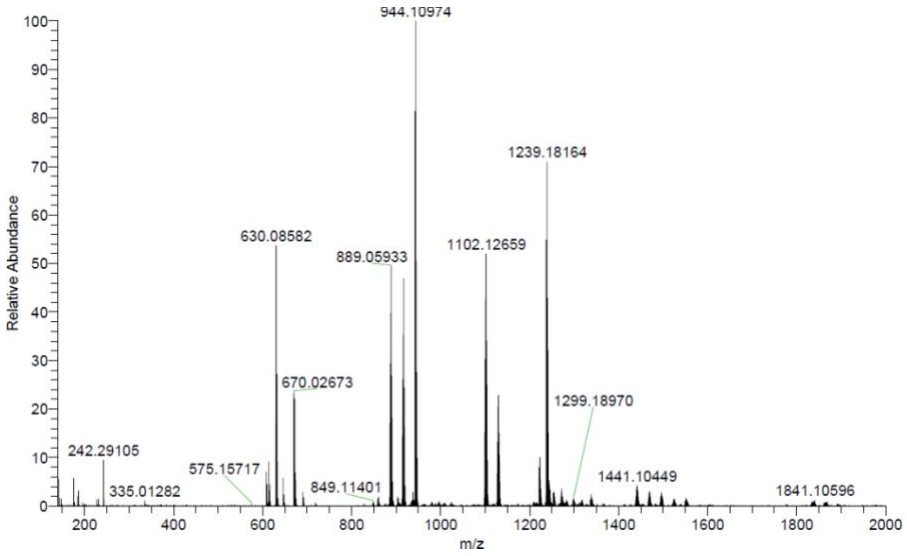

Fig. S19 ESI-MS spectrum of compound **3** in the positive ion mode.

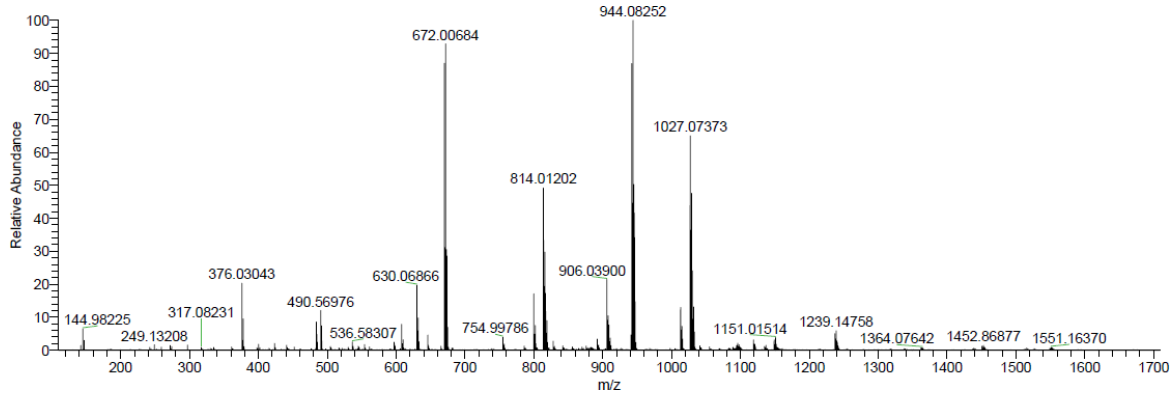

Fig. S20 ESI-MS spectrum of compound **4** in the positive ion mode.

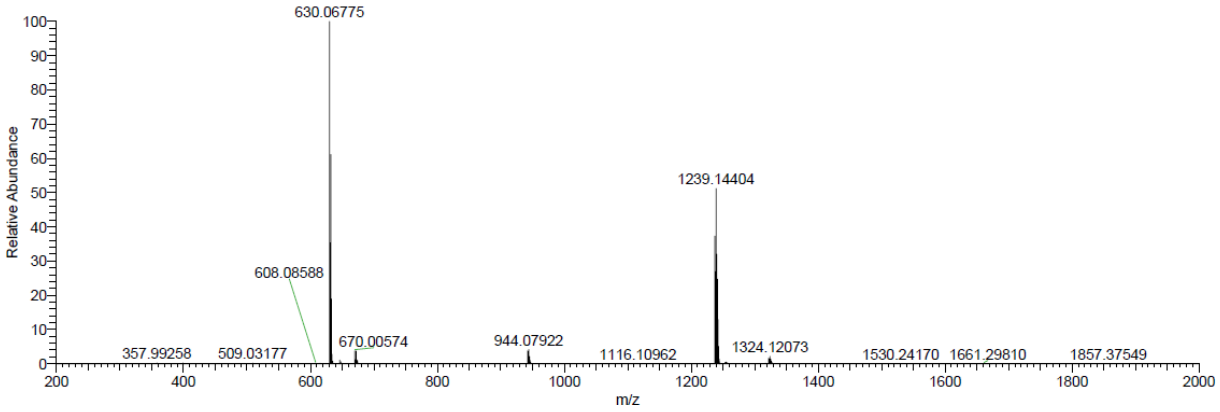

Fig. S21 ESI-MS spectrum of compound **5** in the positive ion mode.

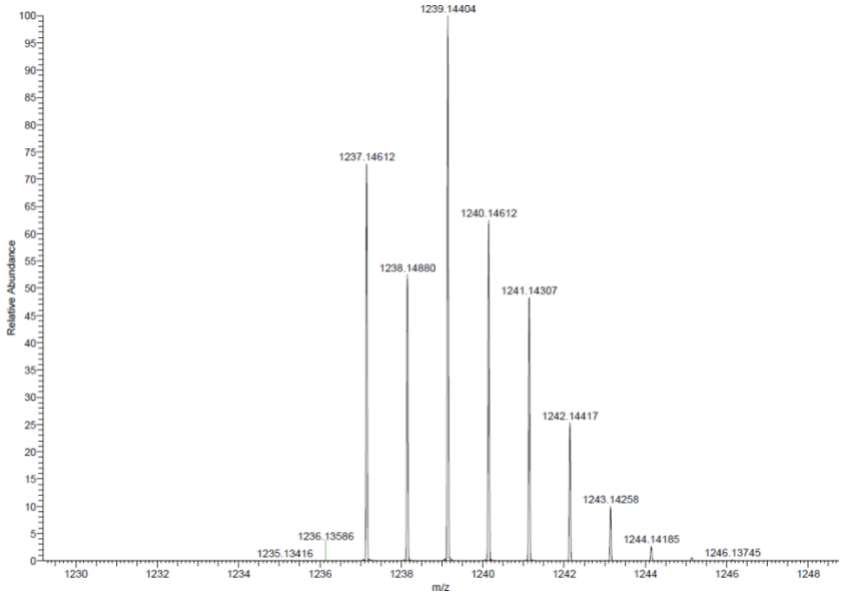

Fig. S22 Zoom of the ESI-MS spectrum of compound **5** in the region about *m*/*z* 1200.

7. Calculated isotopic pattern of compounds 1–5

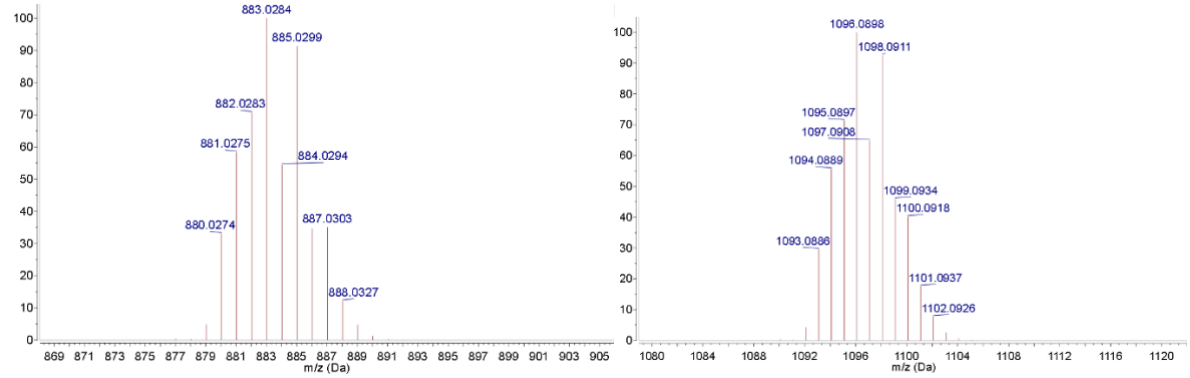

Fig. S23 Calculated isotopic pattern of $[CuGd(L{\cdot}SMe)_2(OOCMe)_2]^+$ (left) and $[CuGd(L{\cdot}SMe)_3(OOCMe)]^+$ (right) fragments in compound **1** (for experiment see Fig. S17).

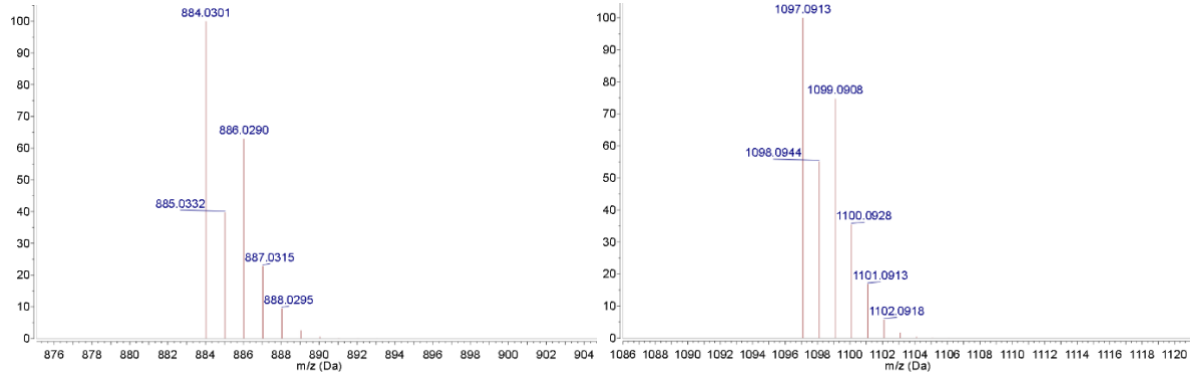

Fig. S24 Calculated isotopic pattern of $[CuTb(L{\cdot}SMe)_2(OOCMe)_2]^+$ (left) and $[CuTb(L{\cdot}SMe)_3(OOCMe)]^+$ (right) fragments in compound **2** (for experiment see Fig. S18).

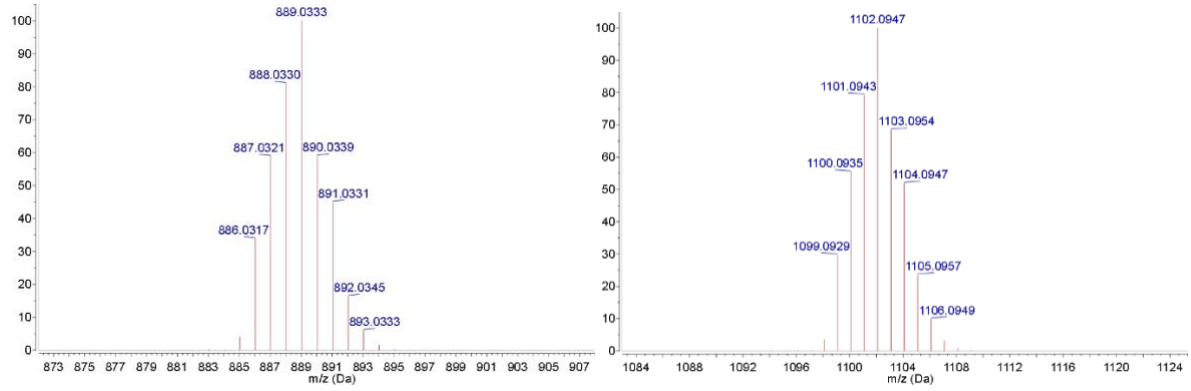

Fig. S25 Calculated isotopic pattern of $[CuDy(L{\cdot}SMe)_2(OOCMe)_2]^+$ (left) and $[CuDy(L{\cdot}SMe)_3(OOCMe)]^+$ (right) fragments in compound **3** (for experiment see Fig. S19).

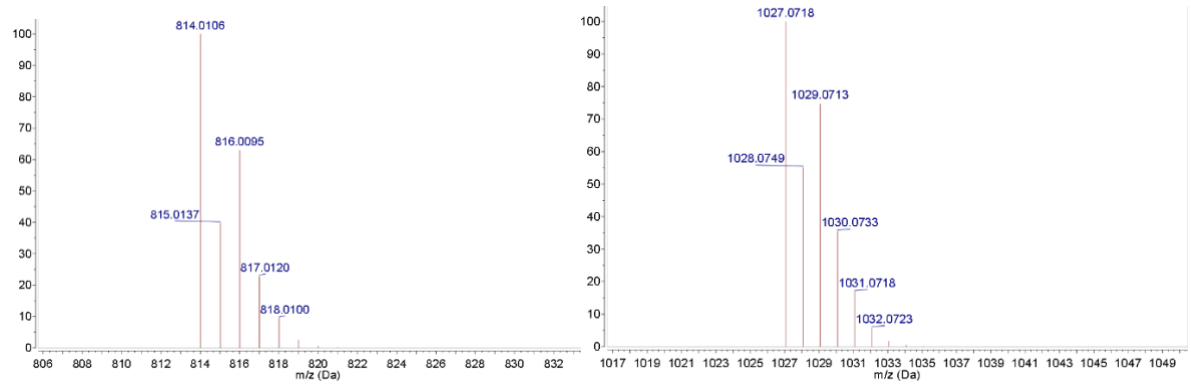

Fig. S26 Calculated isotopic pattern of $[CuY(L{\cdot}SMe)_2(OOCMe)_2]^+$ (left) and $[CuY(L{\cdot}SMe)_3(OOCMe)]^+$ (right) fragments in compound **4** (for experiment see Fig. S20).

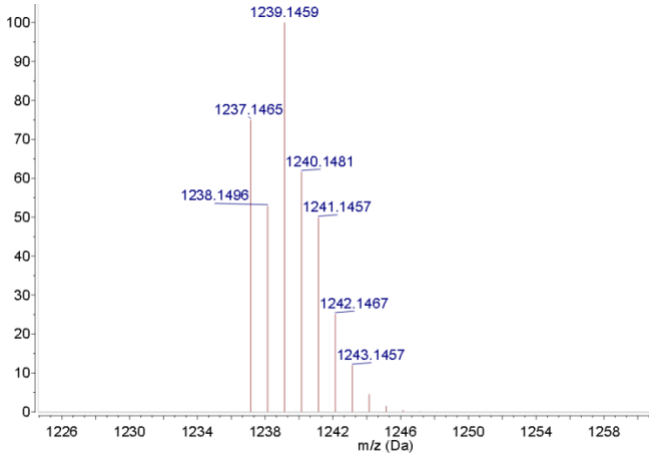

Fig. S27 Calculated isotopic pattern of $[Cu_2Na(L{\cdot}SMe)_4]^+$ fragment in compound **5** (for experiment see Figs. S21 and S22).

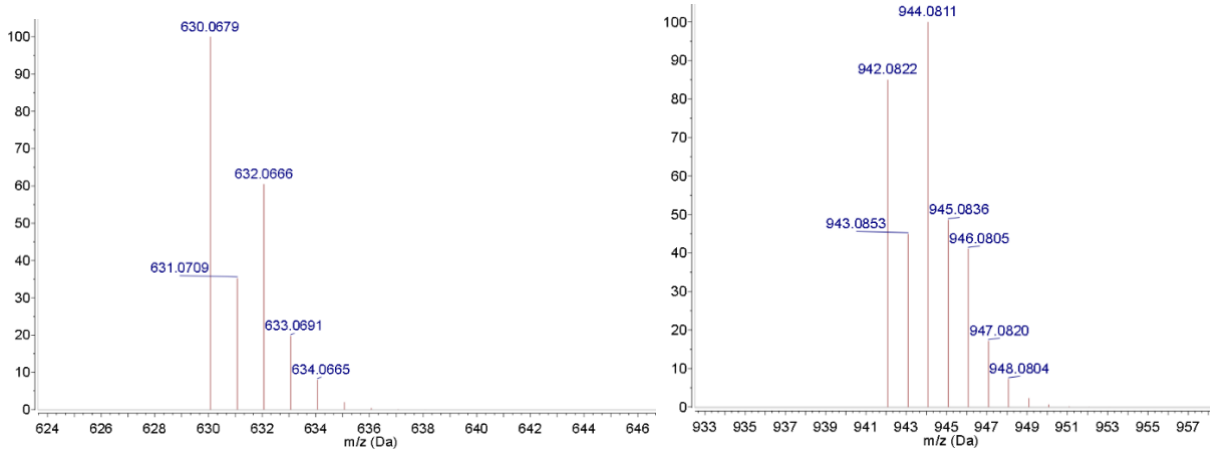

Fig. S28 Calculated isotopic pattern of $[CuNa(L{\cdot}SMe)_2]^+$ (left) and $[Cu_2(L{\cdot}SMe)_3]^+$ (right) fragments in compound **5** (for experiment see Fig. S21).

Table S7 Selected ESI-MS data of compounds **1**–**5**.

Measured [Da]	Calculated [Da]	Sum formula	Composition
883.0308	883.0284	$C_{34}CuGdH_{34}N_2O_8S_2^+$	$[CuGd(L{\cdot}SMe)_2(OOCMe)_2]^+$ (in **1**)
1096.0931	1096.0898	$C_{47}CuGdH_{45}N_3O_8S_3^+$	$[CuGd(L{\cdot}SMe)_3(OOCMe)]^+$ (in **1**)
884.0309	884.0301	$C_{34}CuH_{34}N_2O_8S_2Tb^+$	$[CuTb(L{\cdot}SMe)_2(OOCMe)_2]^+$ (in **2**)
1097.0923	1097.0913	$C_{47}CuH_{45}N_3O_8S_3Tb^+$	$[CuTb(L{\cdot}SMe)_3(OOCMe)]^+$ (in **2**)
889.0593	889.0333	$C_{34}CuDyH_{34}N_2O_8S_2^+$	$[CuDy(L{\cdot}SMe)_2(OOCMe)_2]^+$ (in **3**)
1102.1266	1102.0947	$C_{47}CuDyH_{45}N_3O_8S_3^+$	$[CuDy(L{\cdot}SMe)_3(OOCMe)]^+$ (in **3**)
814.0120	814.0106	$C_{34}CuH_{34}N_2O_8S_2Y^+$	$[CuY(L{\cdot}SMe)_2(OOCMe)_2]^+$ (in **4**)
1027.0737	1027.0718	$C_{47}CuH_{45}N_3O_8S_3Y^+$	$[CuY(L{\cdot}SMe)_3(OOCMe)]^+$ (in **4**)
630.0687–630.0858	630.0679	$C_{30}CuH_{28}N_2NaO_4S_2^+$	$[CuNa(L{\cdot}SMe)_2]^+$ (in **5**)
1239.1440	1239.1459	$C_{60}Cu_2H_{56}N_4NaO_8S_4^+$	$[Cu_2Na(L{\cdot}SMe)_4]^+$ (in **5**)
944.0814–944.1097	944.0811	$C_{45}Cu_2H_{42}N_3O_6S_3^+$	$[Cu_2(L{\cdot}SMe)_3]^+$ (in **5**)

8. TGA curves of compounds 1–5

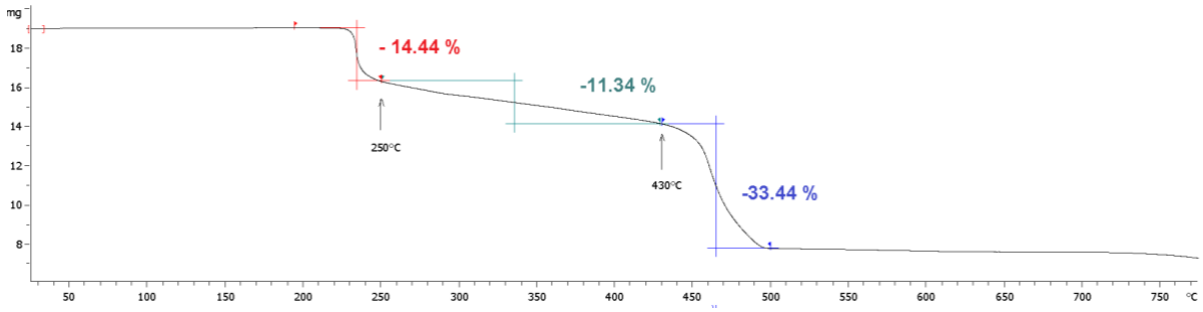

Fig. S29 TGA curve of compound **1** measured in dry air.

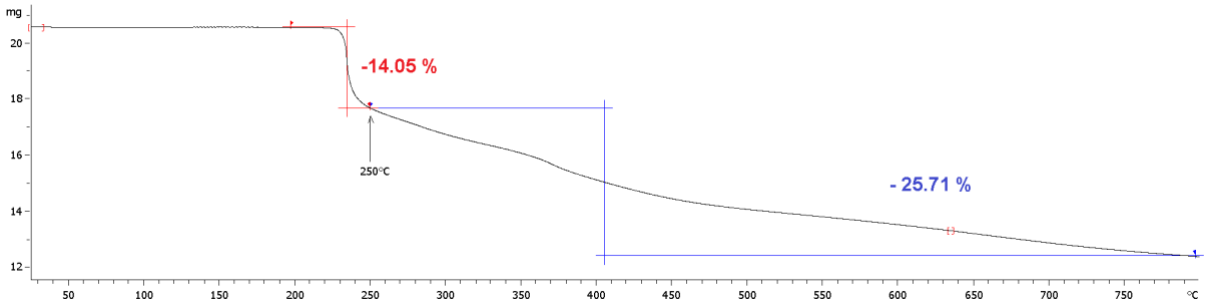

Fig. S30 TGA curve of compound **1** measured under nitrogen atmosphere.

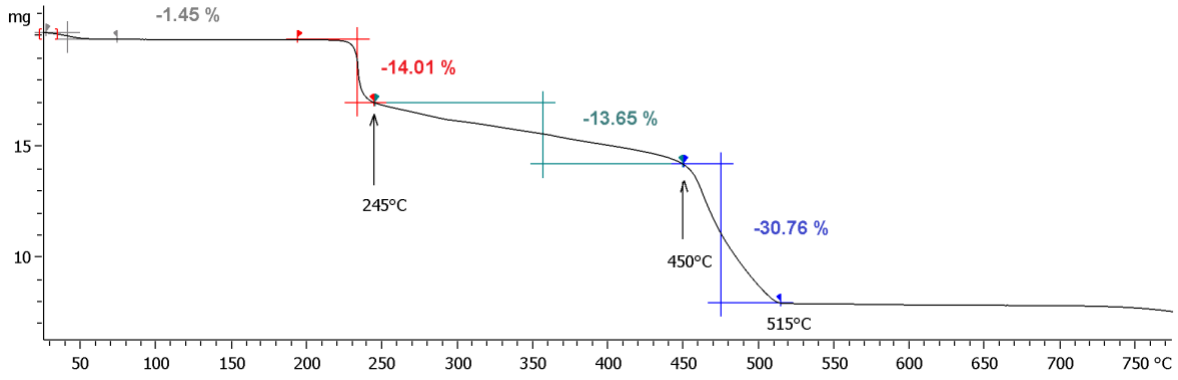

Fig. S31 TGA curve of compound **2** measured in dry air.

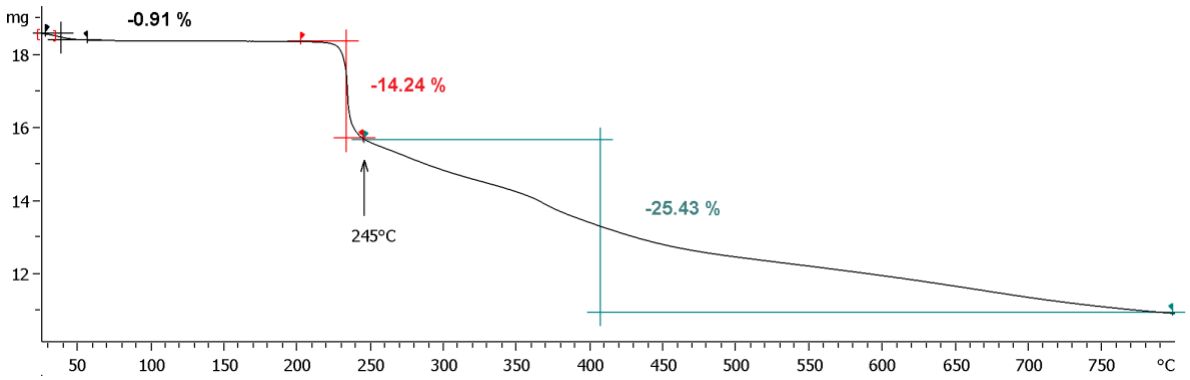

Fig. S32 TGA curve of compound **2** measured under nitrogen atmosphere.

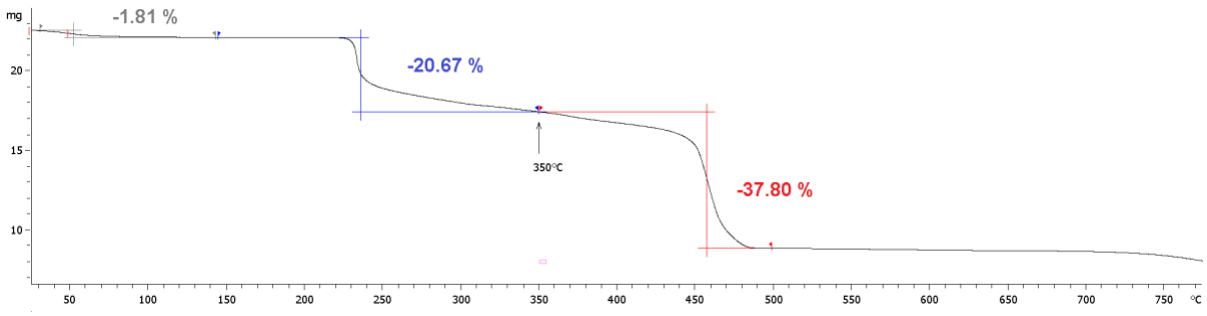

Fig. S33 TGA curve of compound **3** measured in dry air.

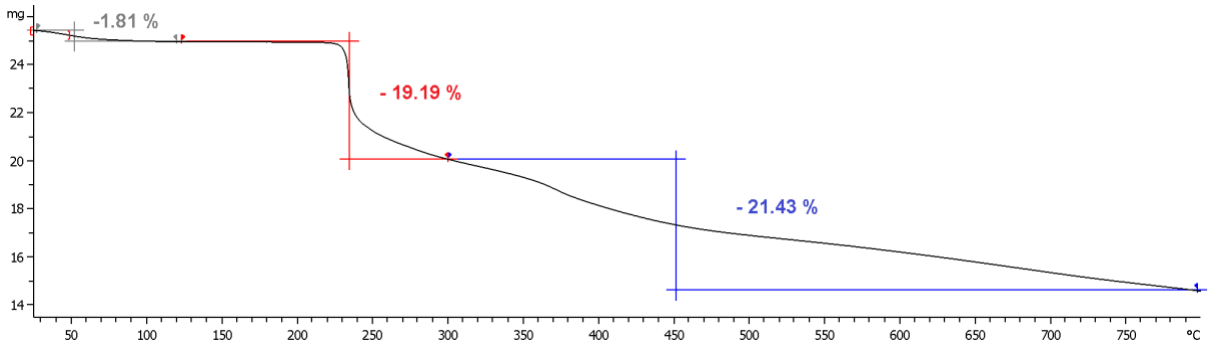

Fig. S34 TGA curve of compound **3** measured under nitrogen atmosphere.

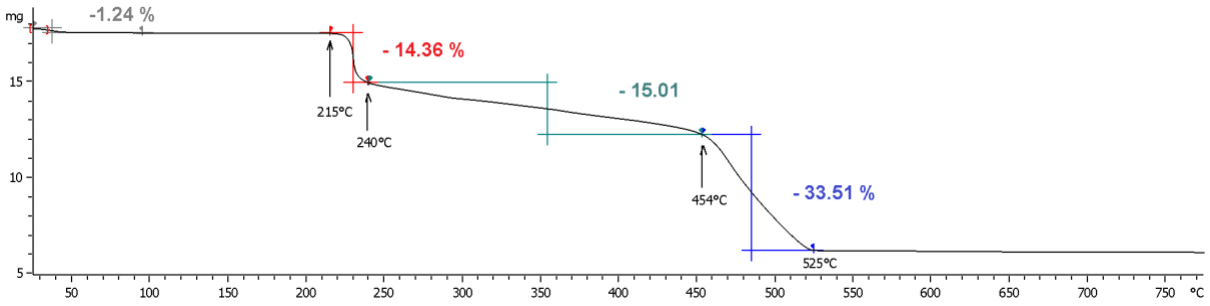

Fig. S35 TGA curve of compound **4** measured in dry air.

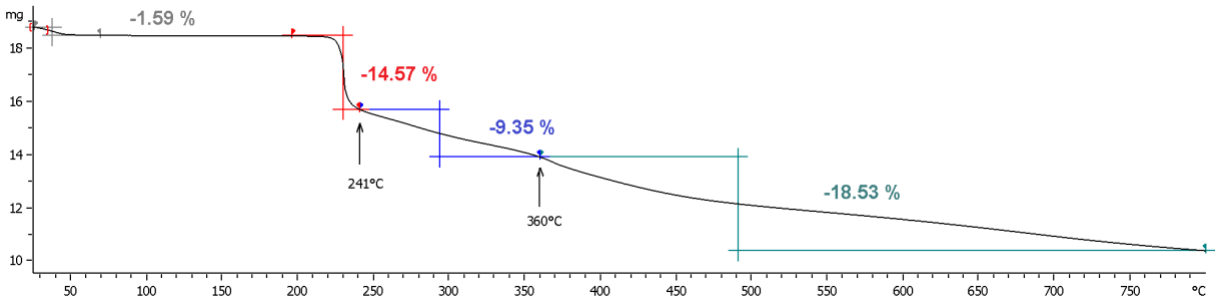

Fig. S36 TGA curve of compound **4** measured under nitrogen atmosphere.

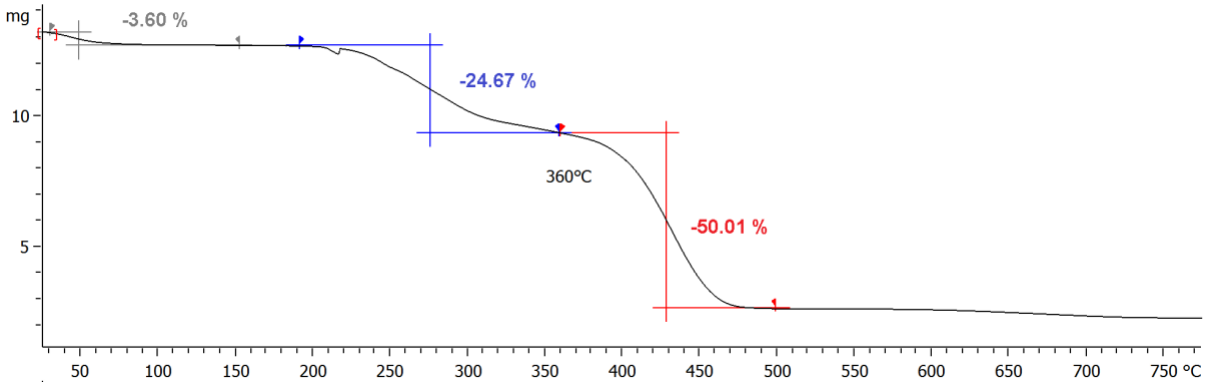

Fig. S37 TGA curve of compound **5** measured in dry air.

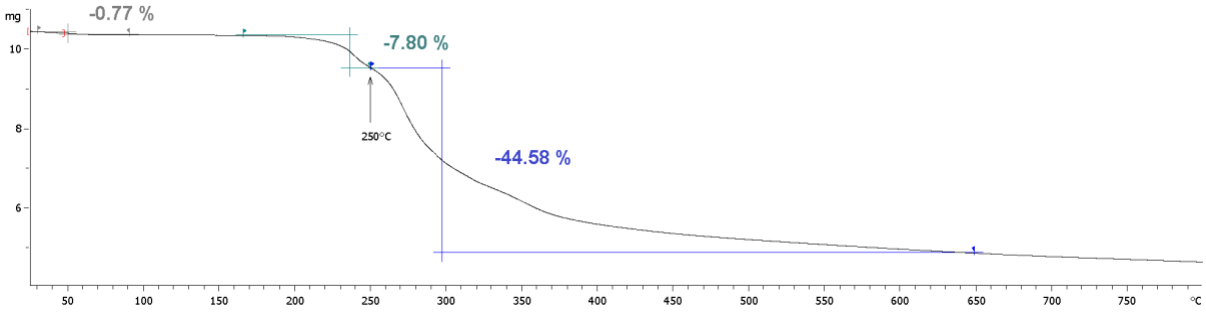

Fig. S38 TGA curve of compound **5** measured under nitrogen atmosphere.

9. Details of large-area transport measurements

Sample preparation

The Au and/or Ag substrates used in this work are made by mechanical Template Stripping (TS) as described elsewhere.[18] In our case, we deposited 100 nm of Au and/or Ag (99.99%) by thermal vacuum deposition onto a 3" Silicon wafer (with no adhesion layer). Using UV-curable Optical Adhesive (OA) Norland 61, 1 cm^2 glass chips were glued on the metal surfaces. The TS procedure provides ultra-flat smooth surfaces, which allows self-assembly process to achieve high yields of working junctions. All samples were made by incubation of freshly cleaved gold slides in ~0.1 mM solutions in methanol at room temperature for ~16 h.

Data acquisition

Data were acquired in a home-built setup that is described in detail elsewhere.[19] Samples were taken out from solution, carefully rinsed with pure methanol and gently blown to dryness with nitrogen. Each SAM was then measured by placing a sharp tip of EGaIn in visual contact with the surface. Histograms of the values of *J* at each value of *V* were then fit to Gaussian distributions to calculate the average value of *J*. No data were discarded during the fitting procedure. Standard deviation of the fits was represented as error bars. Four samples were prepared for each compound and every sample was measured until 10 working junctions were obtained. Working junction is defined as a junction that does not exhibit either a no contact current or a short circuit current. The yields of working junctions for SAMs of each compound **1**–**4** are presented in Table S8. Total mean yield is 67%.

Table S8 Data acquired for compounds **1**–**4**.

Compound	Samples	Contacts	Working junctions	Yield
1	4	65	40	62%
2	4	42	40	95%
3	4	49	40	82%
4	4	82	40	49%

Transition voltages

We calculate transition voltage by re-plotting each I/V trace in Fowler-Nordheim coordinates, $ln(I/V^2)$ versus $1/V$, and found the minimum from the numerical derivative. All values were then

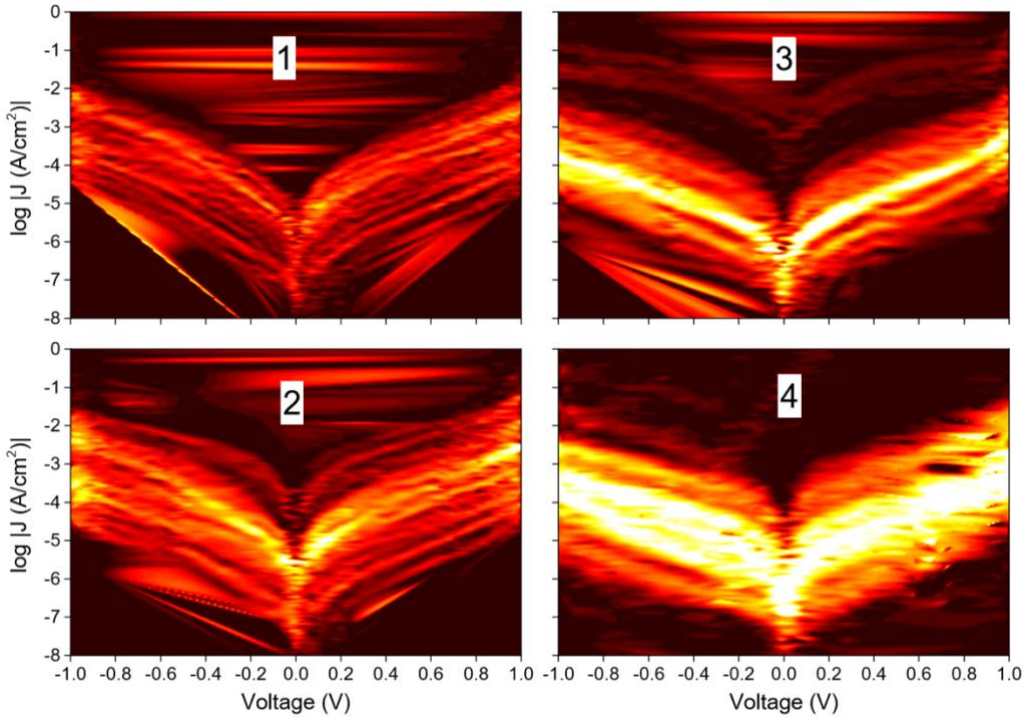

Fig. S39 Raw *log*|*J*| vs *V* data for complexes **1**–**4** presented in the form of heat maps. The heat maps are constructed such that a slice at a certain voltage step represents a histogram of log|J| at this specific voltage. No data were discarded for the construction of heat maps. The straight lines above and below the v-shaped real data (for complexes **1**–**3**) are artifacts from the interpolation procedure.

plotted in a histogram to which a Gaussian distribution was fit to get a peak value and a standard deviation. We used Scientific Python to automate the entire process, providing only raw J/V data as an input. Figure S40 shows the peak values of Gaussian fits along with standard deviation as error bars for the four compounds **1**–**4**. All of them are positioned around ~ 0.3 V with V_T of compound **4** being poorly defined.

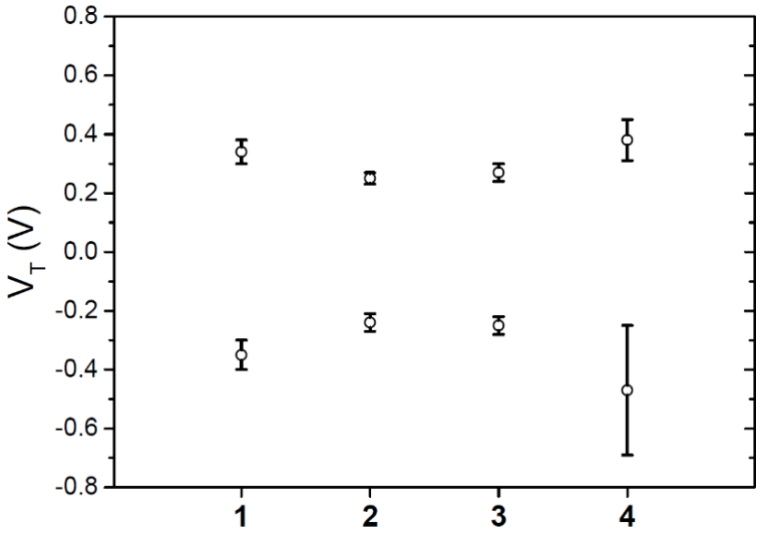

Fig. 40 Average values of V_T of compounds **1**–**4** with standard deviation plotted as error bars. No apparent trend is observed and all values coalesce to ~0.3 V.

Conductance analysis

In order to determine the average conductivity (J_{avg}) for compounds **1**–**4** we combined the values of *J* at –0.5V into a histogram and fit it with a Gaussian distribution (Fig. S41). The peak value was then compared to a series of alkanethiolates on Ag^{TS} (Fig. 7, main text).

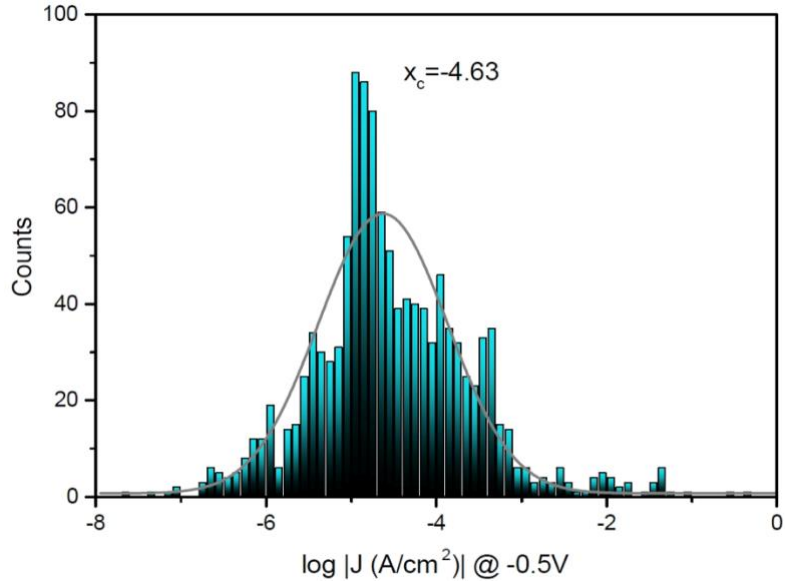

Fig. S41 Combined histogram of log |*J*| at –0.5 V for the compounds **1**–**4** with a Gaussian fit. The peak position corresponds to average conductivity $J_{avg} = -4.63\ A/cm^2$ at –0.5 V.

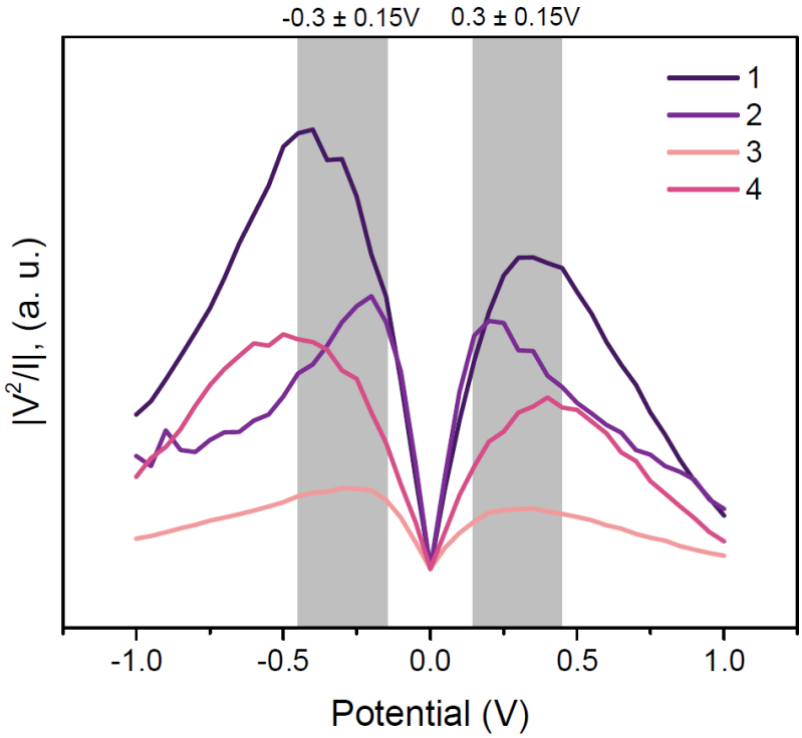

Fig. S42 Transition voltage spectroscopy of complexes **1**–**4**. Visual representation of the average conductance (presented in Fig. 6, main text) replotted in $|V^2/I|$ vs *V* coordinates. Here, peak values correspond to V_T. All values coalesce to ~0.3 V, with V_T of complex **4** being poorly defined, that is a broad distribution with big variance.

STM measurements

The monolayers corresponding to compounds **1**–**4** were studied using scanning tunneling microscopy (STM). A similar method was applied to prepare SAMs of compounds **1**–**4** on commercial Au on mica (Au/mica). The Au/mica samples were immersed in methanolic solutions of **1**–**4** (0.1 mM) overnight inside the glove box where oxygen and water are limited in the ppm level. Then, they were rinsed with methanol and dried with a flow of N_2. Imaging of the samples was performed using Picoscan software by a Molecular Imaging STM set-up under ambient conditions. Cutting Pt/Ir (80/20) tips were used to obtain constant current images at room temperature with a bias voltage applied to the sample. A fresh tip was used for every sample. The STM images are processed and analyzed using the software WSxM 4.0 Beta 9.0. Figure S43 illustrates the obtained STM images. No apparent packing structure can be determined from these images. Compounds **1**–**4** are homogenously distributed on the gold surface and resemble a monolayer.

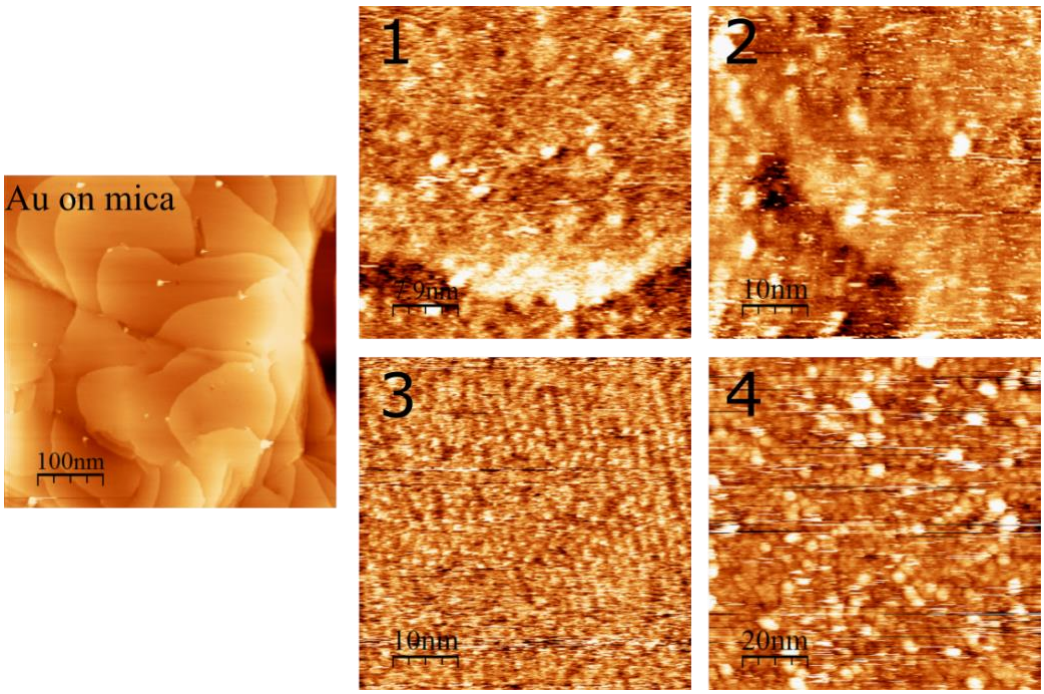

Fig. S43 STM images of the SAMs of bare Au/mica and compounds **1**–**4** on Au/mica, I_t = 10 pA, U_s = 0.8 V, 512 pixel.

Ellipsometry

The SAMs were characterized by ellipsometry. These measurements were acquired on freshly prepared samples in air on a V-Vase Rotating Analyzer equipped with a HS-190 monochromator ellipsometer and calculated via a two-layer model consisting of a bottom Au layer, for which optical constants were calculated from freshly prepared template stripped Au surfaces, and a Cauchy layer

with a chosen value of n = 1.5 an k = 0 at all wavelengths (A=1.5, B=C=0). The results are summarized in Table S9.[20]

Table S9 Ellipsometric thickness (in nm) for the SAMs of compounds **1**–**4**. The average thickness is 1.291 nm.

Compound	Measurement	Ellipsometric thickness
1	1	1.081 ± 0.030
	2	1.085 ± 0.030
2	1	1.312 ± 0.032
	2	1.208 ± 0.033
3	1	1.546 ± 0.029
	2	1.566 ± 0.032
4	1	1.254 ± 0.036
	2	1.274 ± 0.037

10. References

[1] Lueken, H. *Magnetochemie*, Teubner, Stuttgart, **1999**.

[2] Speldrich, M.; Schilder, H.; Lueken, H.; Kögerler, P. A Computational Framework for Magnetic Polyoxometalates and Molecular Spin Structures: CONDON 2.0. *Isr. J. Chem.* **2011**, *51*, 215–227.

[3] van Leusen, J.; Speldrich, M.; Schilder, H.; Kögerler, P. Comprehensive Insight into Molecular Magnetism via CONDON: Full vs. Effective Models. *Coord. Chem. Rev.* **2015**, *289–290*, 137–148.

[4] Griffith, J. S. *The Theory of Transition Metal Ions*, Cambridge University Press, Cambridge, **1980**.

[5] Ramade, I.; Kahn, O.; Jeannin, Y.; Robert, F. Design and Magnetic Properties of a Magnetically Isolated $Gd^{III}Cu^{II}$ Pair. Crystal Structures of $[Gd(hfa)_3Cu(salen)]$, $[Y(hfa)_3Cu(salen)]$, $[Gd(hfa)_3Cu(salen)(Meim)]$, and $[La(hfa)_3(H_2O)Cu(salen)]$ [hfa = Hexafluoroacetylacetonato, salen = *N*,*N*‘-Ethylenebis(salicylideneaminato), Meim = 1-Methylimidazole]. *Inorg. Chem.* **1997**, *36*, 930–936.

[6] Gleizes, A.; Julve, M.; Kuzmina, N.; Alikhanyan, A.; Lloret, F.; Malkerova, I.; Sanz, J. L.; Senocq, F. Heterobimetallic *d–f* Metal Complexes as Potential Single-Source Precursors for MOCVD: Structure and Thermodynamic Study of the Sublimation of $[Ni(salen)Ln(hfa)_3]$, Ln = Y, Gd. *Eur. J. Inorg. Chem.* **1998**, 1169–1174.

[7] Cosquer, G.; Pointillart, F.; Le Guennic, B.; Le Gal, Y.; Golhen, S.; Cador, O.; Ouahab, L. 3d4f Heterobimetallic Dinuclear and Tetranuclear Complexes Involving Tetrathiafulvalene as Ligands: X-ray Structures and Magnetic and Photophysical Investigations. *Inorg. Chem.* **2012**, *51*, 8488−8501.

[8] Zhang, P.; Zhang, L.; Lin, S.-Y.; Tang, J. Tetranuclear $[MDy]_2$ Compounds and Their Dinuclear [MDy] (M = Zn/Cu) Building Units: Their Assembly, Structures, and Magnetic Properties. *Inorg. Chem.* **2013**, *52*, 6595–6602.

[9] Upadhyay, A.; Singh, S. K.; Das, C.; Mondol, R.; Langley, S. K.; Murray, K. S.; Rajaraman, G.; Shanmugam, M. Enhancing the Effective Energy Barrier of a Dy(III) SMM Using a Bridged Diamagnetic Zn(II) Ion. *Chem. Commun.* **2014**, *50*, 8838–8841.

[10] Upadhyay, A.; Komatireddy, N.; Ghirri, A.; Tuna, F.; Langley, S. K.; Srivastava, A. K.; Sañudo, E. C.; Moubaraki, B.; Murray, K. S.; McInnes, E. J. L.; Affronte, M.; Shanmugam, M. Synthesis and Magnetothermal Properties of a Ferromagnetically Coupled Ni^{II}–Gd^{III}–Ni^{II} Cluster. *Dalton Trans.* **2014**, *43*, 259–266.

[11] Bluhm, M. E.; Ciesielski, M.; Görls, H.; Walter, O.; Döring, M. Complexes of Schiff Bases and Intermediates in the Copper-Catalyzed Oxidative Heterocyclization by Atmospheric Oxygen. *Inorg. Chem.* **2003**, *42*, 8878–8885.

[12] Mukherjee, P.; Drew, M. G. B.; Figuerola, A.; Ghosh, A. Incorporation of a Sodium Ion Guest in the Host of Copper(II)-Schiff-Base Complexes: Structural Characterization and Magnetic Study. *Polyhedron* **2008**, *27*, 3343–3350.

[13] Biswas, S.; Naiya, S.; Drew, M. G. B.; Estarellas, C.; Frontera, A.; Ghosh, A. Trinuclear and Tetranuclear Adduct Formation Between Sodium Perchlorate and Copper(II) Complexes of Salicylaldimine Type Ligands: Structural Characterization and Theoretical Investigation. *Inorg. Chim. Acta* **2011**, *366*, 219–226.

[14] Chakrabarty, P. P.; Biswas, D.; García-Granda, S.; Jana, A. D.; Saha, S. Sodium Ion Assisted Molecular Self-Assembly in a Class of Schiff-Base Copper(II) Complexes. *Polyhedron* **2012**, *35*, 108–115.

[15] Maiti, M.; Sadhukhan, D.; Thakurta, S.; Sen, S.; Zangrando, E.; Butcher, R. J.; Deka, R. C.; Mitra, S. Pseudohalide-Controlled Assemblies of Copper–Schiff Base Complexes with an Encapsulated Sodium Ion: Synthesis, Crystal Structure, and Computational Studies. *Eur. J. Inorg. Chem.* **2013**, 527–536.

[16] Biswas, A.; Mondal, S.; Mohanta, S. Syntheses, Characterizations, and Crystal Structures of 3d–s/d^{10} Metal Complexes Derived from Two Compartmental Schiff Base Ligands. *J. Coord. Chem.* **2013**, *66*, 152–170.

[17] Fellah, F. Z. C.; Costes, J.-P.; Duhayon, C.; Vendier, L. Use of Azido Ligands in the Syntheses of Different Homo- and Hetero-Complexes. *Polyhedron* **2016**, *111*, 101–108.

[18] Weiss, E. A.; Kaufman, G. K.; Kriebel, J. K.; Li, Z.; Schalek, R.; Whitesides, G. M. Si/SiO_2-Templated Formation of Ultraflat Metal Surfaces on Glass, Polymer, and Solder Supports: Their Use as Substrates for Self-Assembled Monolayers. *Langmuir* **2007**, *23*, 9686–9694.

[19] Fracasso, D.; Valkenier, H.; Hummelen, J. C.; Solomon, G. C.; Chiechi, R. C. Evidence for Quantum Interference in SAMs of Arylethynylene Thiolates in Tunneling Junctions with Eutectic Ga–In (EGaIn) Top-Contacts. *J. Am. Chem. Soc.* **2011**, *133*, 9556–9563.

[20] Valkenier, H.; Huisman, E. H.; van Hal, P. A.; de Leeuw, D. M.; Chiechi, R. C.; Hummelen, J. C. Formation of High-Quality Self-Assembled Monolayers of Conjugated Dithiols on Gold: Base Matters. *J. Am. Chem. Soc.* **2011**, *133*, 4930–4939.